ACS NANO

www.acsnano.org

Radiotherapy-Triggered In Situ Tumor Vaccination Boosts Checkpoint Blockaded Immune Response via Antigen-Capturing Nanoadjuvants

Pei Xu,[‖] Jie Ma,[‖] Yang Zhou,* Yuan Gu, Xiaju Cheng, Yangyun Wang, Yong Wang,*
and Mingyuan Gao*

Cite This: *ACS Nano* 2024, 18, 1022−1040

Read Online

ACCESS | Metrics & More | Article Recommendations | Supporting Information

ABSTRACT: **In situ vaccination (ISV) formed with the aid of intratumorally injected adjuvants has shed bright light on enhancing the abscopal therapeutic effects of radiotherapy. However, the limited availability of antigens resulting from the radiotherapy-induced immunogenic cell death largely hampers the clinical outcome of ISV. To maximally utilize the radiotherapy-induced antigen, we herein developed a strategy by capturing the radiotherapy-induced antigen in situ with a nanoadjuvant comprised of CpG-loaded Fe_3O_4 nanoparticles. The highly efficient click reaction between the maleimide residue on the nanoadjuvant and sulfhydryl group on the antigen maximized the bioavailability of autoantigens and CpG adjuvant in vivo. Importantly, combined immune checkpoint blockade can reverse T cell exhaustion after treatment with radiotherapy-induced ISV, thereby largely suppressing the treated and distant tumor. Mechanistically, metabolomics reveals the intratumorally injected nanoadjuvants disrupt redox homeostasis in the tumor microenvironment, further inducing tumor ferroptosis after radiotherapy. Overall, the current study highlights the immense potential of the innovative antigen-capturing nanoadjuvants for synergistically enhancing the antitumor effect.**

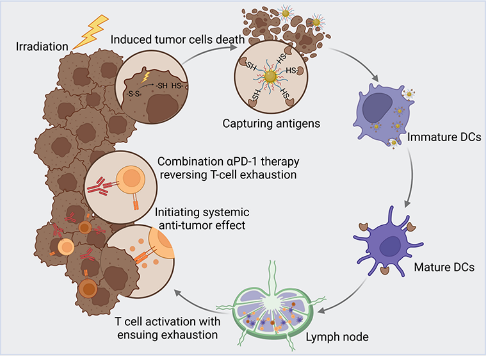

KEYWORDS: *in situ vaccination, antigen capture, tumor radiotherapy, PD-1 blockade, T cell exhaustion*

INTRODUCTION

Cancer immunotherapy has indeed made significant advancements in the clinic, and immune checkpoint blockade therapies have emerged as highly effective treatments for certain types of cancer.[1,2] However, it is important to note that not all cancer patients respond favorably to these therapies, especially those with immunologically "cold" tumors that are characterized by limited immune cell infiltration and low neo-antigen availability.[3]

Alternative vaccines have shown promise in enhancing antitumor immunity by utilizing exogenous tumor antigens combined with adjuvants.[4] The main objective in designing tumor vaccines is to deliver substantial amounts of high-quality antigens to dendritic cells (DCs) within the tumor, thereby eliciting adaptive T cell responses.[5] Despite several decades of efforts, the FDA has only approved one autologous DCs vaccine loaded with a specific tumor-associated antigen (TAA), known as sipuleucel-T.[6] The limited progress can be largely attributed to various challenges faced by the current tumor vaccines,[7,8] including tumor heterogeneity with diverse somatic mutations, unsatisfactory delivery efficiency, DCs dysfunction, and the immune escape of tumors via programmed death ligand-1/programmed death 1 (PD-L1/PD-1) signaling pathway. In situ vaccination (ISV) is becoming an increasingly attractive strategy that combines tumor autoantigens, derived from immunogenic cell death (ICD) induced by radiotherapy or chemotherapy, with immunostimulants.[9,10] It offers potential for overcoming tumor heterogeneity and eliciting a systemic antitumor immune response capable of targeting unrecognized metastases in a personalized manner.[11−14] Until now, numerous clinical or preclinical trials have been focused

Received: October 19, 2023
Revised: December 16, 2023
Accepted: December 19, 2023
Published: December 22, 2023

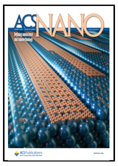

https://doi.org/10.1021/acsnano.3c10225

Scheme 1. Mechanism of the Proposed Antigen-Capturing ISV in Combination with PD-1 Blockade to Reverse T Cell Exhaustion[a]

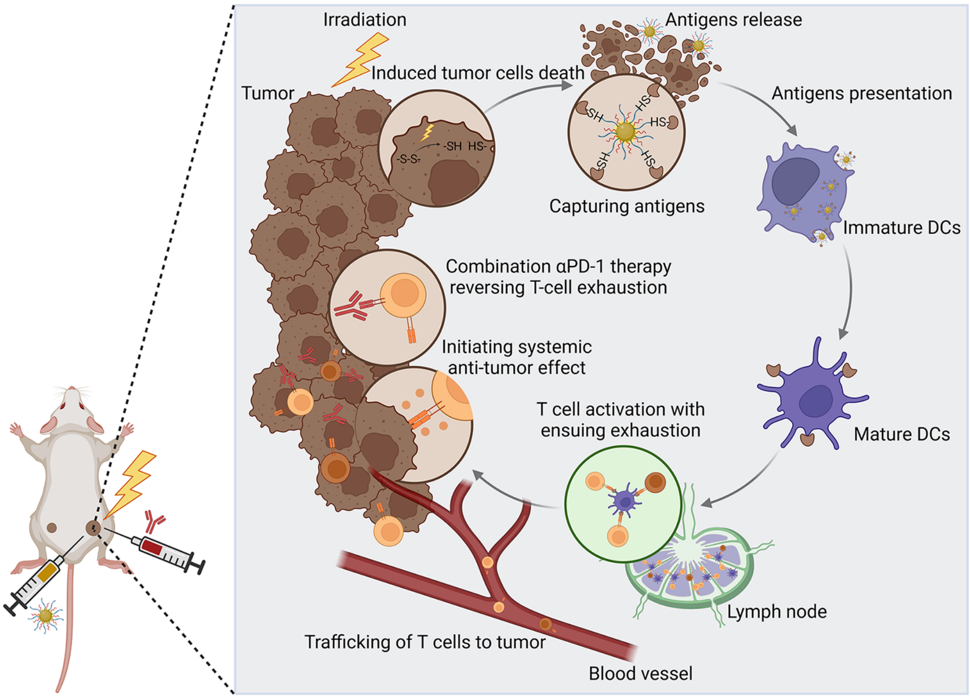

[a] Created with BioRender.com.

on ISV induced by radiotherapy.[15,16] For example, in combination with intratumorally injected CpG oligonucleotide, an agonist of Toll-like receptor 9 (TLR9), radiotherapy was demonstrated to induce regression at the treated tumor site as well as significant shrinkage at distant tumor site.[15] Researchers at the Icahn School of Medicine at Mount Sinai also proposed a radiotherapy-induced ISV that involved repeated intratumoral injections of Fms-like tyrosine kinase 3 ligands to recruit DCs into tumor, followed by multiple intratumoral injections of a TLR3 agonist to activate DCs.[16] However, the development of ISV is confronted by limitations regarding the availability of vaccine components within the tumor microenvironment due to the rapid metabolism and enzymatic degradation of antigens and adjuvants.[17] To overcome these challenges, there is a need to exert spatial and temporal control over the interactions between vaccine components and immune cells, aiming to orchestrate a potent and durable immune response.

The utilization of biomaterials as delivery carriers for ISV holds significant promise for enhancing their efficacy of tumor immunotherapy by mitigating the off-target toxicity of vaccines.[18] Various biomaterials have been explored for delivering antigens and adjuvants, including oncolytic viruses,[19] viral-like particles,[20] polymer nanoparticles,[21,22] etc. A noteworthy advancement in this field is the particle surface chemistry-dependent antigen-capturing pioneered by Wang and co-workers,[23] which has been demonstrated to have improved abscopal therapeutic effects of radiotherapy. Following this strategy, Morris et al. developed a radiotherapy-induced ISV using multiple adjuvant-loaded antigen-capturing nanoparticles.[24] Despite these advancements, it is fascinating to explore the dynamic regulation of the tumor microenvironment by carrier materials and how it impacts immune responses of radiotherapy.[25] Understanding this relationship is crucial for differentiating immune responses in treated and distant tumors, especially in poorly immunogenic tumors with limited immune recognition and response.[26] Furthermore, prolonged exposure to antigenic stimulation through radiotherapy can enhance T cell clonality and enrich for CD8$^+$ T cells with an exhausted phenotype,[27] where effector functions decline and inhibitory receptors like PD-1, CTLA-4, and Tim-3 are upregulated on the T cell surface.[28,29] To address T cell exhaustion and boost immune responses, immune checkpoint blockade therapy has shown promise by blocking inhibitory receptors like PD-1 and CTLA-4, thereby restoring T cell function.[30−32] Additionally, ISV strategies are being explored to revitalize T cell responses and overcome exhaustion.[33] In order to maximize the efficacy of ISV and other immune-based therapies, it is indeed crucial to initiate the early reversal of T cell exhaustion. By addressing T cell exhaustion at an early stage, we can restore the functionality of T cells and enhance their effectiveness in fighting against cancer. This can potentially improve the outcomes of ISV and other immunotherapies, particularly in cases where there are limitations in the immune recognition and response of poorly immunogenic tumors.

Herein, we developed maleimide-grafted polyethylene glycol and CpG comodified Fe_3O_4 nanoadjuvants, denoted and further abbreviated as Fe_3O_4@Mal/CpG and FMC, respectively, for forming visualizable radiotherapy-induced ISV through magnetic resonance imaging (MRI), as shown in Scheme 1. In this design, the magnetic iron oxide nanoparticles served as both carrier and adjuvant. The resulting FMC nanoadjuvants were expected to capture sulfhydryl-bearing TAAs, formed in response to radiotherapy, through the surface maleimide residues. It was demonstrated that ISV exhibited prolonged retention time within tumors. The flow cytometry and in vivo immunoimaging revealed that the expression of

https://doi.org/10.1021/acsnano.3c10225
ACS Nano 2024, 18, 1022−1040

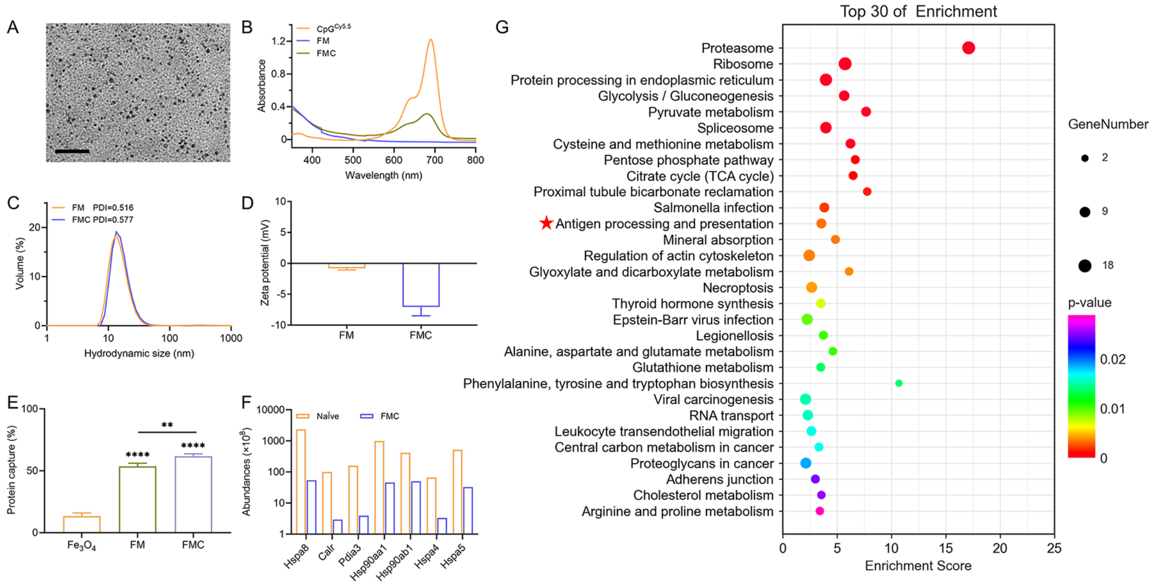

Figure 1. Characterization of FMC and antigens capture. (A) TEM image of FMC (scale bar equals to 50 nm). (B) UV−vis absorption spectra of FM, CpG$^{Cy5.5}$, and FMC$^{Cy5.5}$. (C) Hydrodynamic size distribution profiles of FM and FMC. (D) ζ potentials of FM and FMC. (E) Antigen capturing efficiency for Fe_3O_4 nanoparticles, FM and FMC. (F) Relative abundance of proteins associated with antigen processing and presentation pathways. (G) KEGG enrichment analysis of the first 30 proteins. Statistical differences were obtained by one-way analysis of variance (ANOVA). *P* values: *, $P < 0.05$; **, $P < 0.01$; ***, $P < 0.005$; ****, $P < 0.001$.

PD-1 on T cells in tumors was increased after treatment, which confirmed that the highly efficient delivery of antigens by ISV led to T cell exhaustion, encouraging us to perform a PD-1 blockade to reverse T cell exhaustion during in vivo treatment. The significant MRI signal changes of tumor site were observed in vivo, suggesting that the ISV disrupts the redox homeostasis in the tumor microenvironment. The following metabolomic analysis indicated that the FMC-based ISV induced perturbations in amino acid metabolism, enabling the differentiation of immune responses between local and distant tumors. These findings highlight the significance of the antigen-capturing FMC nanoadjuvants for synergistic radio-immunotherapy of tumors.

RESULTS AND DISCUSSION

Preparation and Characterization of FMC. CpG oligodeoxynucleotides can induce the immune response of DCs through TLR9 signaling pathway.[34] To enable effective endocytosis of the negatively charged CpG by DCs, a carrier for CpG is essentially required. In this respect, biocompatible Fe_3O_4 nanoparticles were adopted as the carrier, through an asymmetric polyethylene glycol 2000 (PEG2000) ligand bearing a maleimide group at one end and a diphosphate group at the other end (Mal-PEG-Dp), to load thiolated CpG. Transmission electron microscopy (TEM) analysis revealed that the average size of the CpG-loaded Fe_3O_4 nanoparticles is 3.9 ± 0.6 nm, showing good monodispersity as given in Figure 1A. To confirm the successful loading of CpG, Cy5.5-modified CpG (CpG$^{Cy5.5}$) was used instead of CpG to characterize the resulting FMC through conventional electron spectroscopy. As shown in Figure 1B, the absorption of FMC$^{Cy5.5}$ exhibits the characteristic peaks to CpG$^{Cy5.5}$, and the loading efficiency of CpG in FMC was estimated to be around 22% according to the results in Supporting Information Figure S1A,B. The molar ratio of Fe^{2+} to CpG$^{Cy5.5}$ in FMC was around 3:1 (Figure S1C). The hydrodynamic size and ζ potential of FMC were determined to be 12.3 ± 0.3 nm and −7.1 ± 1.4 mV, respectively, as shown in Figure 1C,D.

In Vitro Antigen Capturing by FMC. To investigate the potential impact of irradiation (IR) on antigen release and sulfhydryl group exposure, 5,5′-dithiobis-2-nitrobenzoic acid was used to quantitatively determine the sulfhydryl groups present in the supernatant of 4T1 breast cancer cells obtained after irradiation treatment. Through absorption spectroscopy shown in Figure S2A,B, approximately 0.2 μmol of sulfhydryl residues were detected in the supernatant of 3×10^6 4T1 cells treated by 6 Gy of IR.

To further validate the capacity of FM and FMC for capturing tumor antigens, PEGylated Fe_3O_4 nanoparticles bearing no maleimide group were prepared and used as a control. As shown in Figure 1E, FM and FMC capture 3 times more tumor antigens than the control nanoparticles. Meanwhile, the hydrodynamic size and ζ potential of the FMCs were increased from 12.3 ± 0.25 to 52.3 ± 18.6 nm and from −7.06 ± 1.42 to −2.5 ± 0.4 mV, respectively, after co-incubation with supernatants of irradiated 4T1 cells (Figure S2C,D). In addition, FMC exhibited a capability for capturing proteins from a broad type of tumor cells that were treated with irradiation followed by lysis (Figure S2E). Mass spectrometry analysis shown in Figure S2F was performed to identify the components of the proteins captured. The results indicated that over 286 types of proteins from the cell supernatants were captured. Damage-associated molecular pattern proteins (DAMPs) belong to a broad class of pro-inflammatory molecules that can enhance the immune responses. As shown in Figure 1F, several typical DAMPs are found to be captured by FMC, including members of the heat shock protein (Hsps) family, calreticulin (Calr), and protein disulfide isomerase A3 (Pdia3). Furthermore, a Kyoto Encyclopedia of Genes and Genomes (KEGG) pathway enrichment analysis and abundance statistics were also conducted (Figure 1G), and the results indicated that the top 30 captured proteins were involved in antigen processing

https://doi.org/10.1021/acsnano.3c10225
ACS Nano 2024, 18, 1022−1040

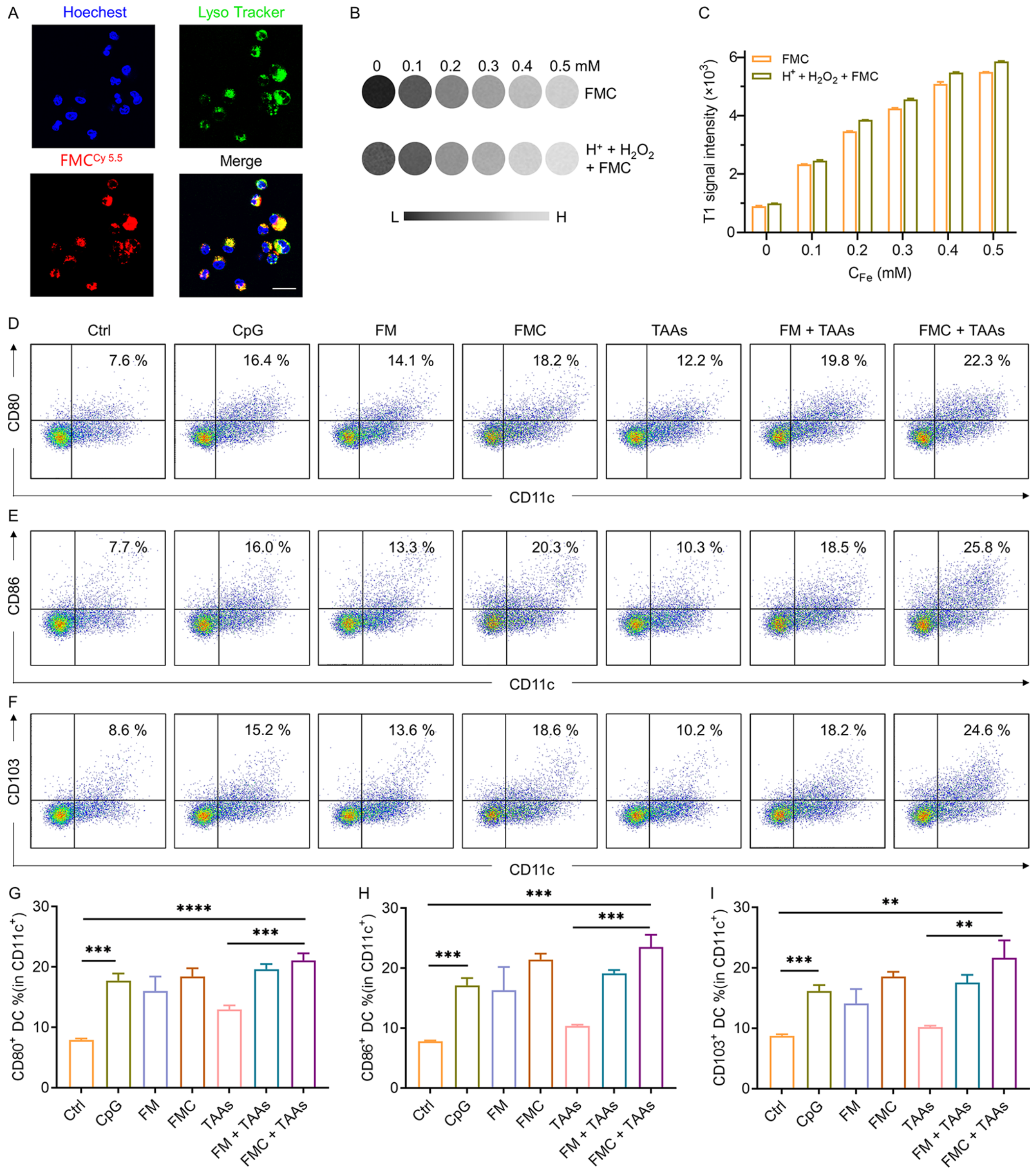

Figure 2. Impacts of FMC-based ISV on tumor microenvironment and activation of BMDCs in vitro. (A) Confocal microscopy images of BMDCs obtained after incubation with FMC$^{Cy5.5}$ followed by staining for showing nuclear (Hoechest) and endolysosome (Lyso Tracker) (scale bar equals to 20 μm). (B) MR images of FMC with different concentrations and in different microenvironments. (C) Quantification of MRI signals. (D−F) Flow cytometry results of CD11c$^+$CD80$^+$ DCs (D) CD11c$^+$CD86$^+$ DCs (E) and CD11c$^+$CD103$^+$ DCs (F) after receiving different treatments. (G, H) Quantification of the maturation of BMDCs from different treatment groups. (I) Quantitative expression levels of CD11c$^+$CD103$^+$ DCs. Statistical differences were obtained by one-way analysis of variance (ANOVA). *P* values: *, $P < 0.05$; **, $P < 0.01$; ***, $P < 0.005$; ****, $P < 0.001$.

and presentation. These findings confirmed that FMC can capture TAAs to form TAA-loaded FMCs that were expected to activate the immune responses.

Activation of BMDCs by FMC-Based ISV In Vitro. DCs play a crucial role in the immune system by sensing innate danger signals and coordinating the adaptive immune response against foreign invaders apart from processing and presenting antigens.[35] Previous studies have shown that CpG can be internalized into endosomes of DCs to activate them through the intracellular TLR9 receptor.[36] To investigate whether TAA-loaded FMC can be taken up and processed by bone marrow-derived dendritic cells (BMDCs), FMC$^{Cy5.5}$ and TAA-loaded FMC$^{Cy5.5}$ were co-incubated with BMDCs for 24 h. The localization of FMC within BMDCs was observed using laser confocal microscopy. The results in Figures 2A and S3A show that FMC are internalized into BMDCs and localized within lysosomes. The uptake efficiency of free CpG$^{Cy5.5}$, FMC$^{Cy5.5}$, and TAA-loaded FMC$^{Cy5.5}$ by BMDCs was characterized by flow cytometry. As shown in Figure S3B, the uptake efficiency of TAA-loaded FMC was 1.2- and 1.1-fold that of free CpG and FMC, respectively.

To further explore the fate of FMC within the lysosomes of BMDCs, in vitro lysosome simulation experiments were conducted. In brief, FMC was exposed to an acidic medium containing H_2O_2 to simulate the lysosome microenvironment. The T1MRI signal displayed an increasing trend in the simulated lysosome microenvironment, as shown in Figure 2B,C, probably because the Fenton reaction between Fe^{2+} and

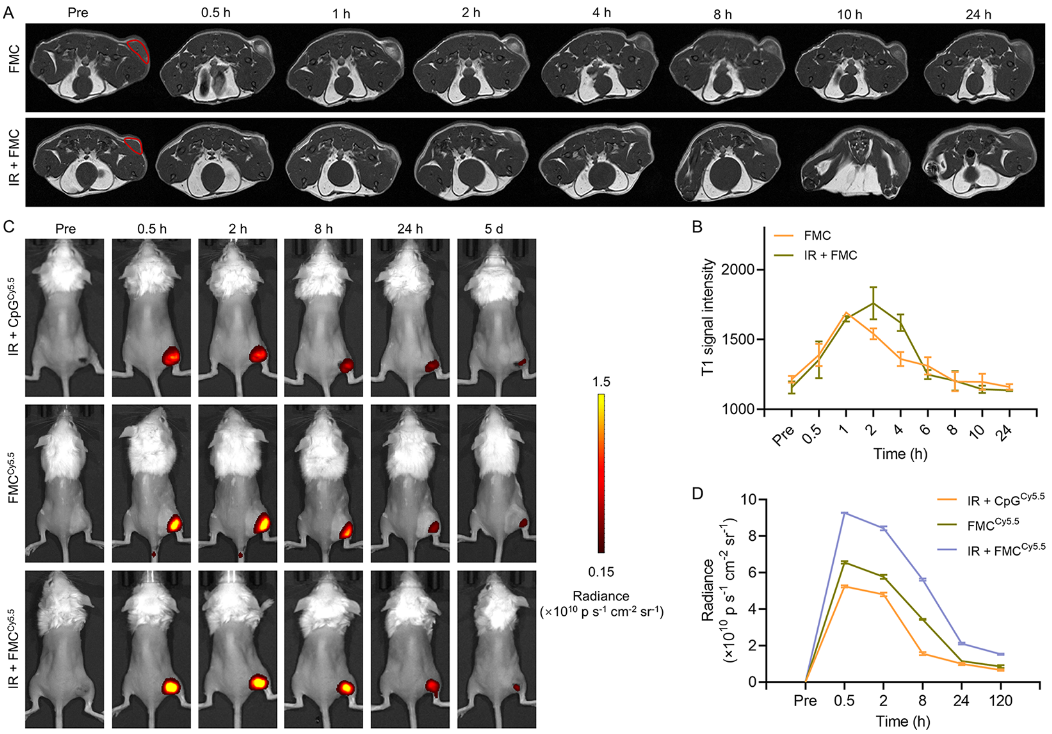

Figure 3. Fate of FMC in vivo. (A) T1-weighted MR images of mice treated with FMC group and IR + FMC group, respectively. (B) Quantified MR signals of different groups. (C) Distribution of CpG$^{Cy5.5}$ and FMC$^{Cy5.5}$ in vivo after different treatments. (D) Temporal radiance recorded from different groups. Statistical differences were obtained by one-way analysis of variance (ANOVA). *P* values: *, $P < 0.05$; **, $P < 0.01$; ***, $P < 0.005$.

H_2O_2 converts Fe^{2+} into Fe^{3+}. The higher number of unpaired electrons of Fe^{3+} results in a shorter T1 relaxation time and higher T1 signal intensity. Thus, it is reasonable to infer that the FMC-based ISV may have the potential to dissociate at the lysosome and activate DCs.

To confirm the ability of FMC-based ISV for activating BMDCs, BMDCs were cocultured with CpG, TAAs, FM, FMC, TAA-loaded FM, and TAA-loaded FMC, respectively. As shown in Figure 2D,E, the expression levels of the surface activation markers of BMDCs, i.e., CD80 and CD86, are significantly increased in the above-mentioned groups, if compared with that of the control group (PBS). Of particular interest, the flow cytometry data presented in Figure 2G,H demonstrate that BMDCs treated with TAA-loaded FMC exhibit expression CD80 and CD86 levels approximately two times higher than those of the control group. It is known that CD103$^+$ DCs secrete chemokines such as CXCL9 and CXCL10 that facilitate antigen cross-presentation and recruitment of tumor-reactive T cells.[37] Therefore, the expression of CD103 by BMDCs from each treatment group was also compared. As shown in Figure 2F,I, the CD103 level of BMDCs treated with TAA-loaded FMCs is increased by a factor of ~2 in comparison with the control group, similar to the situations for CD80 and CD86. All of these results collectively demonstrate that FMCs are capable of capturing antigens to effectively activate DCs and promote antigen presentation.

In Vivo Fate of FMC-Based ISV. Based on the T1 signal variations observed in the simulated lysosome microenvironment in vitro, the in vivo behavior of FMC-based ISV with the aid of X-ray IR was also investigated. The T1 signal of the tumor site was recorded at different time points after intratumoral injection of FMC. As shown in Figure 3A,B, the T1 signal of FMC group reaches its maximum 1 h postinjection. In contrast, the IR + FMC group exhibits the T1 signal peak at 2 h postinjection. Subsequently, both of these two groups show gradually decreased T1 signals to reach baseline levels 24 h postinjection. These T1 signal variations indicate that the FMC-based Fenton reaction taking place within the tumor can be potentially enhanced by X-ray IR.

To further explore the fate of FMC-based ISVs in vivo, fluorescence imaging studies were carried out on mice intratumorally injected with FMC$^{Cy5.5}$ and CpG$^{Cy5.5}$ after being irradiated by 6 Gy of X-ray, respectively. To show the IR effects, mice intratumorally injected with FMC$^{Cy5.5}$, but receiving no IR treatment, were also used as the control group. As shown in Figure 3C,D, FMC$^{Cy5.5}$ exhibits a stronger fluorescence signal that lasts up to a week within the tumor, contrasting to the rapidly metabolized CpG$^{Cy5.5}$. In addition, combining IR with FMC$^{Cy5.5}$ further increases the fluorescence intensity by approximately 30% compared to that with no IR experiment. One week after the intratumoral injection of FMC$^{Cy5.5}$, the mice from the experimental group and control groups were dissected, and their tissues were subjected to ex vivo fluorescence imaging. Figure S4A revealed that a more pronounced Cy5.5 signal was presented by tumors treated with FMC$^{Cy5.5}$ and IR, indicating that the FMC can effectively prolong the intratumoral retention time of CpG, particularly after capturing the released antigens induced by X-ray IR. This indirect evidence strongly suggests that the antigen may have been retained in the tumor for an extended period. Furthermore, it was observed that FMC$^{Cy5.5}$ was primarily eliminated via the kidney.

In Vivo Immune Responses of FMC-Based ISV. ISV was demonstrated to promote the maturation of BMDCs in vitro and exhibit long retention within tumors, which lays a solid

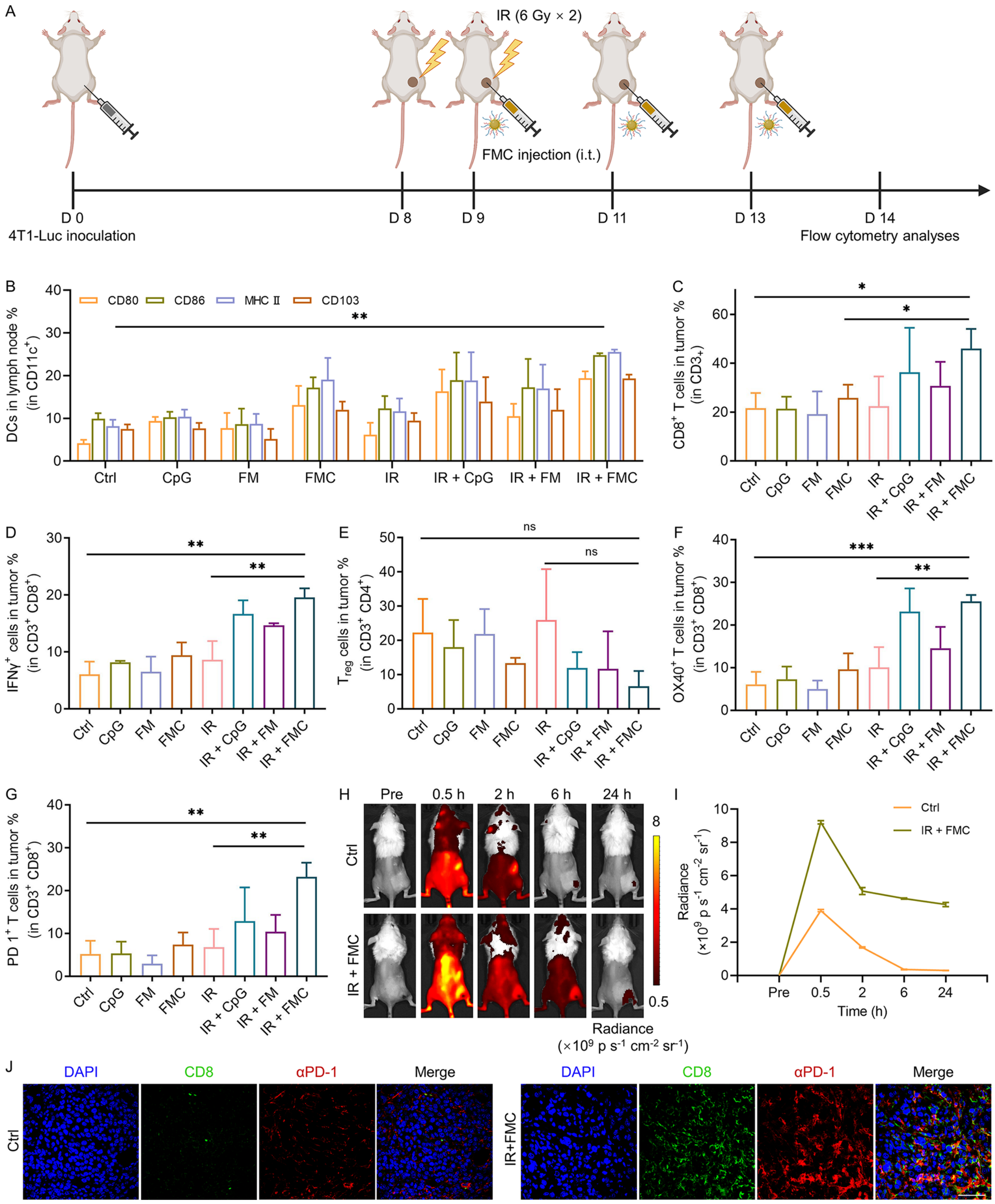

Figure 4. Immune activation effects of FMC-based ISV in vivo. (A) Design of experiments for showing the immune responses induced by FMC-based ISV. Created with BioRender.com. (B) Percentage of DCs (gated on CD11c$^+$) in tumor-draining lymph nodes obtained after different treatments. (C−G) Contents of CD8$^+$ T cell (C), IFN-γ secreting CD8$^+$ T cells (D), Tregs (E), OX40$^+$ T cells (F), and PD-1$^+$ T cells (G) subpopulations in tumors receiving different treatments, determined through flow cytometry analysis. T cells were defined as being CD3$^+$CD8$^+$. (H) Fluorescence imaging of Cy5-αPD-1 in vivo. (I) Temporal fluorescence intensity of the tumor site in vivo. (J) Representative fluorescence images of tumor tissue slices obtained after staining. CD8$^+$ cells, αPD-1, and nuclei are stained green (FITC), red (Cy5), and blue (DAPI), respectively (scale bar corresponds to 50 μm). Statistical differences were obtained by one-way analysis of variance (ANOVA). *P* values: *, $P < 0.05$; **, $P < 0.01$; ***, $P < 0.005$.

corner stone for in vivo immune activation. According to the procedures shown in Figure 4A, subcutaneous 4T1-Luc breast tumor models were established, and the mice received two rounds of irradiation with 6 Gy of X-ray on the tumor sites, followed intratumoral injection of FMC. This group is denoted as the IR + FMC group. For comparison, control (PBS), CpG, FM, FMC, IR, IR + CpG, and IR + FM groups were also included in the experiment. Finally, flow cytometry analysis

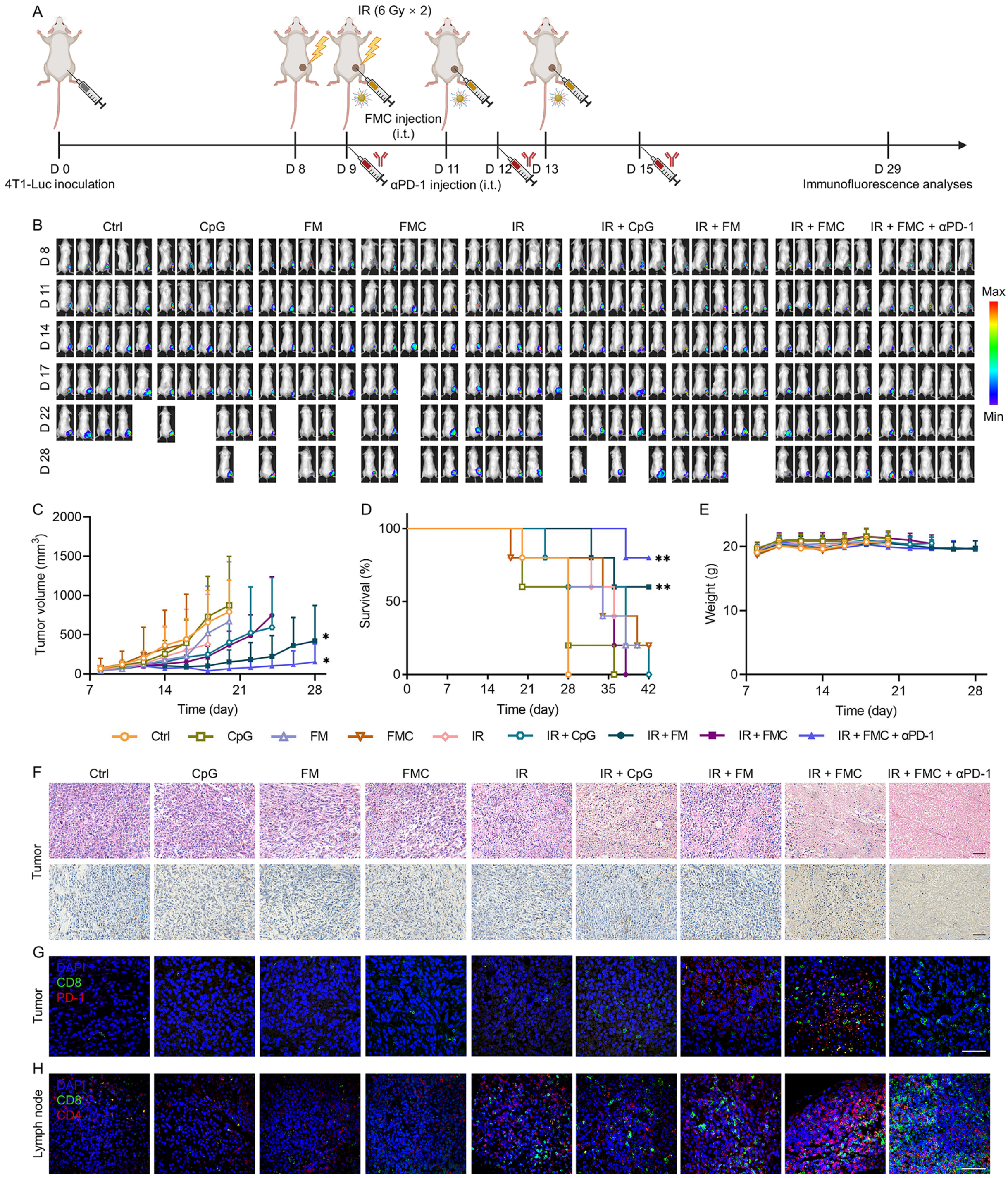

Figure 5. Antitumor effects of FMC-based ISV combined with αPD-1. (A) Schematic illustration showing the design of experiments. Created with BioRender.com. (B) In vivo bioluminescence images of mice in different groups ($n = 5$). Tumor growth curves (C), survival rates (D), and temporal body weight (E) of mice ($n = 5$) from different groups. (F) Representative H&E and TUNEL images of tissue slices of tumors from different treatment groups (scale bar represents 50 μm). (G) Representative fluorescence images of tumor sections in different treatment groups. CD8$^+$ cells, PD-1$^+$ cells, and nuclei in the tumors are shown by the dyes FITC (green), Cy3 (red), and DAPI (blue), respectively (scale bar is 50 μm). (H) Representative fluorescence images of lymph node sections from different treatment groups, with CD8$^+$ cells, CD4$^+$ cells, and nuclei stained green (FITC), red (Cy3), and blue (DAPI), respectively (scale bar equals to 50 μm). Tumor growth was compared by two-way ANOVA with Bonferroni correction. Differences in survival rate were determined for each group by the Kaplan−Meier method, and the overall P value was calculated by the log-rank test. P values: *, $P < 0.05$; **, $P < 0.01$; ***, $P < 0.005$.

was conducted to assess DC maturation in the tumor-draining lymph nodes and T cell activation within the tumors. As shown in Figure 4B, CD80, CD86, MHC II, and CD103 expression in DCs of the IR + FMC group was obviously increased in comparison to those from the other groups. As shown in Figure 4C,D, the total count of CD8$^+$ T cells in the tumor microenvironment in the IR + FMC group is increased by a factor of 1−2 in comparison to those of IR + CpG and control

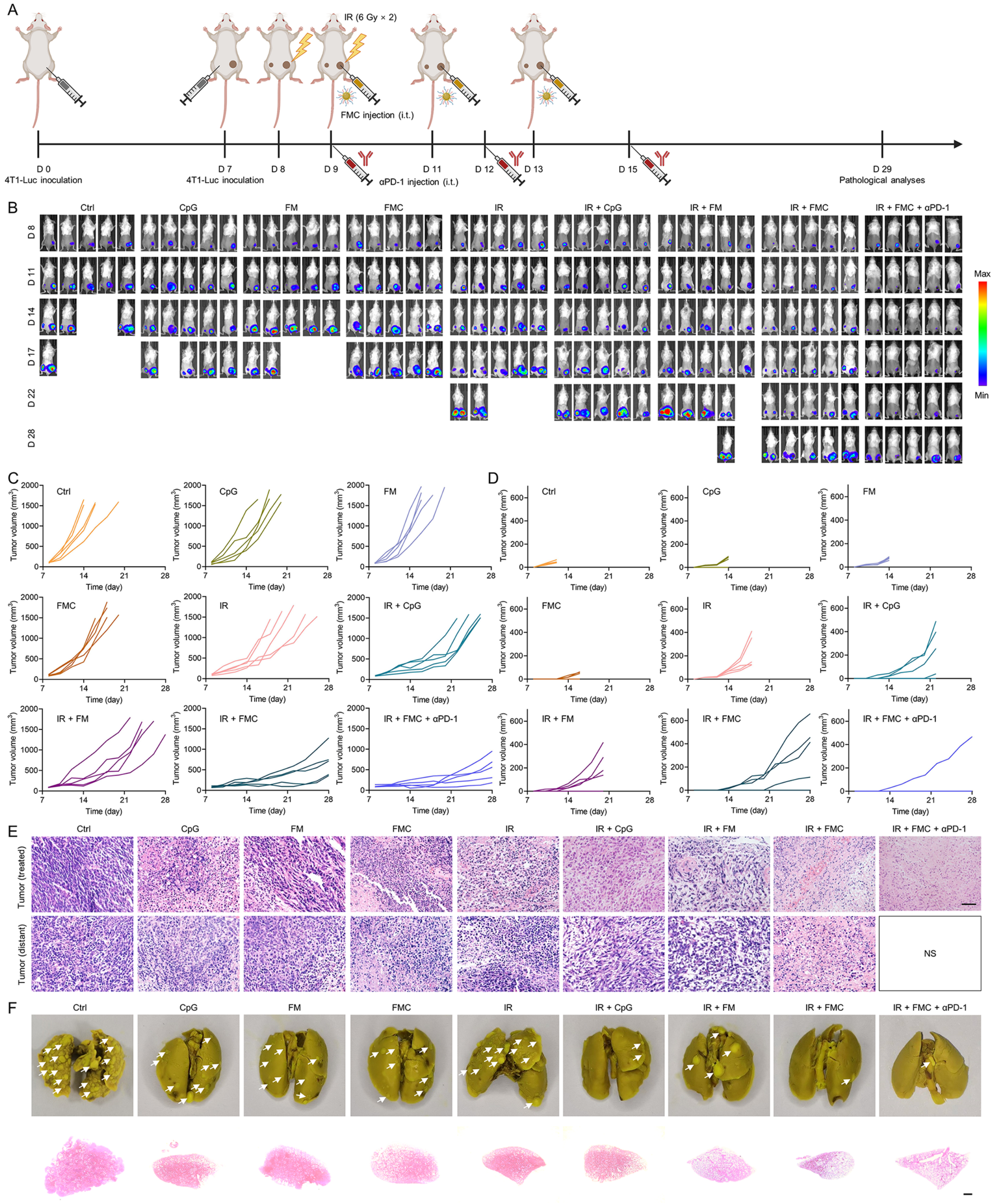

Figure 6. Inhibition effects of bilateral tumor by FMC-based ISV combined with αPD-1. (A) Schematic illustration showing the design of experiments. Created with BioRender.com. (B) In vivo bioluminescence images of mice in different groups ($n = 5$). (C) Growth curves of the treated tumor in different groups ($n = 5$). (D) Growth curves of the distant tumor in different groups ($n = 5$). (E) Imaging of H&E staining of the treated tumor and distant tumor from different groups (scale bar = 50 μm; NS, no sample). (F) Representative photographs showing the tumor nodules in the lungs and representative lung tissues stained with H&E (scale bar = 1000 μm).

groups. In addition, the effector IFN-γ^+ CD8$^+$ T cells are the most abundant in the IR + FMC group. Different from CD8$^+$ T cells, the number of regulatory T (Treg) cells in the tumor of the IR + FMC group is significantly reduced, as shown in Figure 4E. In contrast, IR alone increases the proportion of Treg cells due to the radiotherapy-triggered immunosuppressive effect. Additionally, the expression of surface markers IFN-γ and OX40 on CD4$^+$ or CD8$^+$ T cells is significantly improved after the ISV treatment (Figure 4F and S5A). FMC-based ISV can capture and efficiently deliver antigens, but this process potentially lead to continuous stimulation of antigens and thus induce T cell exhaustion,[38] so the PD-1 expression of T cell exhaustion marker was also examined. It is surprisingly discovered that the IR + FMC group presents a PD-1 expression level in CD8$^+$ T cells approximately 3-fold higher than that of the control group (Figure 4G), which may lead to CD8$^+$ T cell exhaustion and immune evasion.

To further confirm the elevation of the PD-1 level of CD8$^+$ T cells in the tumor microenvironment, in vivo immunofluorescence imaging studies, based on Cy5-labeled PD-1 monoclonal antibody (Cy5-αPD-1), were performed on the control and IR + FMC groups. The preparation of Cy5-αPD-1 was validated by using UV−vis absorption and fluorescence spectroscopy (Figure S6A,B). One week after the subcutaneous breast tumors were treated with IR + FMC, the mice were intravenously injected with Cy5-αPD-1 and then subjected to fluorescence imaging at different time points (Figure 4H). A stronger fluorescence signal can be observed in the tumors of the IR + FMC group compared to the control group (Figure 4I). After 24 h of in vivo imaging studies, the mice of both groups were sacrificed and organs were harvested for ex vivo imaging. Figure S7 showed that the Cy5-αPD-1 signal was present in the liver and kidney of both groups, but the signal was stronger in the tumor and tumor-draining lymph nodes of the IR + FMC group. Immunofluorescence analysis of tumor tissues further confirmed higher infiltration of CD8$^+$ T cells was presented by IR + FMC group in comparison to the control group, evidenced by the colocalization of Cy5-αPD-1 and CD8$^+$ T cells (Figure 4J). Concurrently, the tumor growth curves aligned well with the flow cytometry results, and the IR + FMC group exhibited a significant inhibitory effect on tumor growth (Figure S8A,B). Most importantly, the mice did not display significant changes in body weight during the treatment period, indicating the good safety of the FMC agent (Figure S8C).

Antitumor Effects of FMC-Based ISV and PD-1 Blockade In Vivo. Early exhausted T cells can regain their proliferation and immune effects after being reversed by PD-1 antibody.[39] To evaluate the therapeutic effects of the FMC-based ISV and reverse the exhaustion of T cells, a treatment plan was scheduled on the mouse bearing 4T1-Luc breast tumors, as illustrated in Figure 5A. The experimental groups remained the same as the previously described ones for in vivo immune activation assays, with a new combined treatment group denoted as IR + FMC + αPD-1 being introduced. The tumor growth in each group was monitored by bioluminescence, and the volume was determined every other day. The bioluminescence imaging results presented in Figure 5B demonstrate that IR + FMC and IR + FMC + αPD-1 exhibit the most effective therapeutic effects among all groups. Notably, 60% of tumor-bearing mice achieved complete remission (CR) after receiving IR + FMC in combination with αPD-1. Additionally, the tumor growth curves in Figure 5C reveal that the therapeutic effects of FMC-based ISV can be further enhanced when combined with αPD-1. It can be observed from the survival data that the tumors from the control group reach a volume of 1500 mm^3 within 20 days, while it takes 32 and 38 days for those from IR + FMC and IR + FMC + αPD-1, respectively, as shown in Figure 5D. Importantly, during these treatments, no significant toxicity was observed, as indicated by the stable body weight of the mice over time (Figure 5E).

To further assess the therapeutic efficacy of FMC-based ISV, histological analysis through hematoxylin−eosin (H&E) staining and immunofluorescence analysis were conducted on tumor tissues at the end of the therapeutic experiments. The H&E staining given in Figure 5F reveals that evident tumor necrosis with a more pronounced effect is presented by IR + FMC + αPD-1 group. Moreover, the TUNEL staining for showing apoptotic cells demonstrated that the IR + FMC treatment group exhibited significant tumor cell death compared to the control group. This effect was further enhanced when combined with αPD-1. At the same time, PD-1 positive T cells were reduced in tumors in the FMC-based ISVs treated group, demonstrating that T cell exhaustion was reversed (Figure 5G). In addition, immunofluorescence staining of tumor-draining lymph nodes shows that FMC-based ISVs can effectively induce the infiltration of T cells (Figure 5H). These results support the idea that the FMC-based ISV has the ability to activate innate and adaptive immunity, leading to substantial inhibition of tumor growth in vivo.

Inhibition Metastatic Breast Tumors Using FMC-Based ISV Combined with αPD-1. Metastasis of tumors and the subsequent poor prognosis of patients are the leading causes of tumor-related deaths, with approximately 90% of patients succumbing to tumor metastasis.[40] Encouraged by the promising efficacy observed in the treatment of tumors with FMC-based ISV combined with αPD-1, we further investigated the abscopal antitumor effects of the combined therapy on advanced breast tumors with distant lesions. The treatment plan is shown in Figure 6A. The breast tumor cells were subcutaneously inoculated on the right flank of the mice to establish a tumor. Then, a second tumor was inoculated on the left flank of the mice after the first one reached a volume of 100 mm^3, typically 7 days postinoculation. After that, the tumor on the right flank was treated with CpG, FM, FMC, IR, IR + CpG, IR + FM, IR + FMC, and IR + FMC + αPD-1, respectively, and named as treated tumor hereafter, while the tumor on the left flank remained untreated and named as distant tumor. The bioluminescence imaging results for monitoring the tumor growth are presented in Figure 6B. The survival studies reveal that mortality started to appear 2 weeks postinoculation from the control group, with all mice perishing within 3 weeks. Similarly, the bilateral tumors in the experimental groups, including those treated with CpG, FM, and FMC, respectively, exhibited uncontrolled growth, which resulted in the death of mice on week 3 of postinoculation. The IR + CpG group exhibited no suppression effect on the treated tumor, and the distant tumors continued to grow until all mice succumbed approximately one month after tumor inoculation. However, the IR + FMC group showed superior inhibitory capability against both the treated and distant tumors, particularly when combined with αPD-1 therapy. This improved performance for tumor suppression is obvious in the growth curves of the treated tumors in Figures 6C and S9A, which is consistent with the results of the unilateral tumor experiments. The noteworthy therapeutic efficacy is further supported by the mouse survival rates of different treatment regimens (Figure S9B). However, significant inhibition of the distant tumors was obtained through IR + FMC and IR + FMC + αPD-1 treatments, and an impressive inhibition rate of up to 80% was achieved by IR + FMC + αPD-1, as depicted in Figures 6D and S9C. Pathological analysis of tumor tissues through H&E staining, as shown in Figure 6E, corroborates the experimental findings mentioned above, revealing a substantial reduction in both the treated and distant tumors in the IR + FMC group. Notably, only one sample showing distant tumors is not

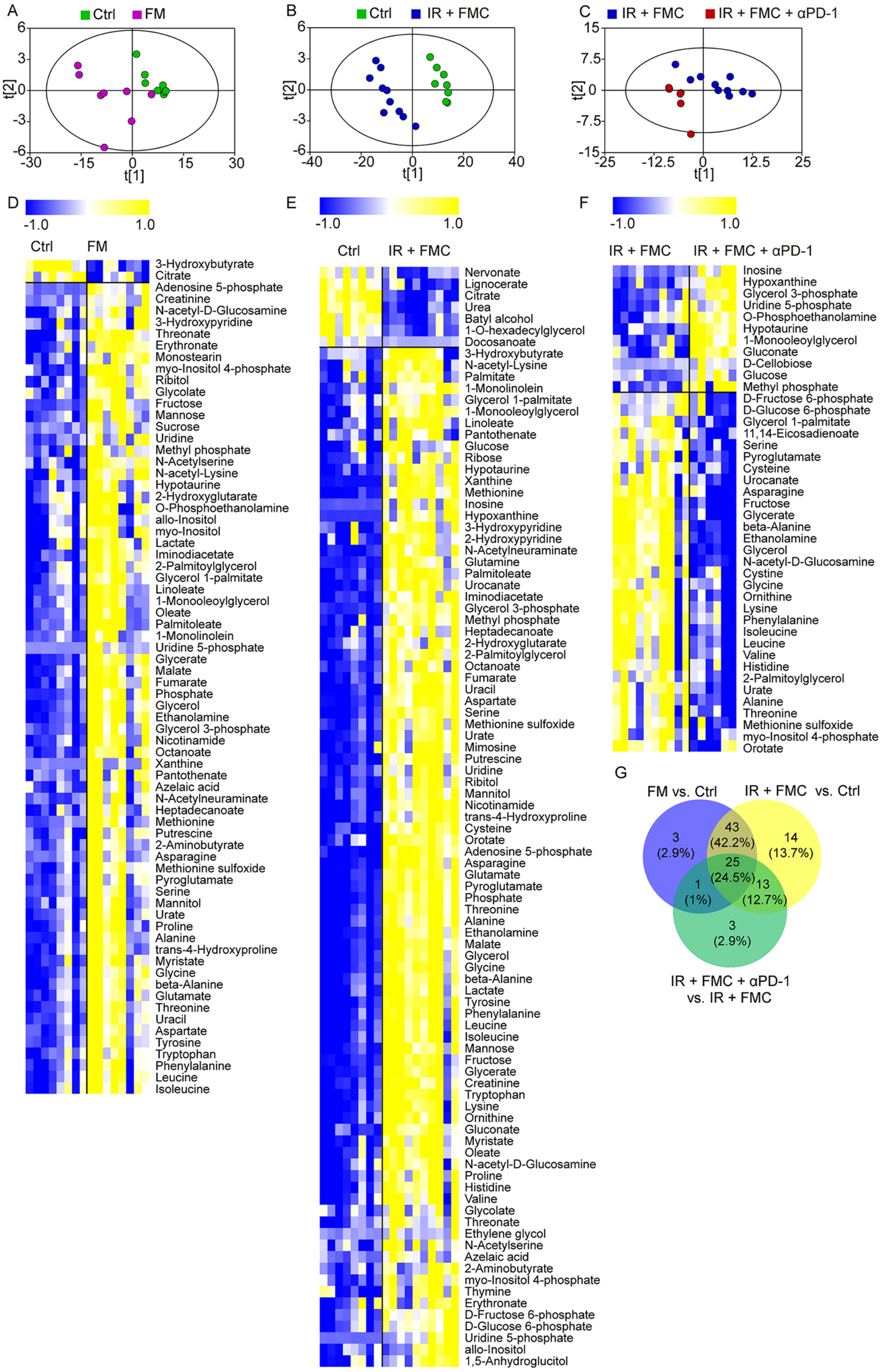

Figure 7. Metabolic profiles of the treated tumor. (A−C) PLS-DA score plot of FM and control group (R2X = 0.826, R2Y = 0.733, and Q2 = 0.525), IR + FMC, and control group (R2X = 0.875, R2Y = 0.959, and Q2 = 0.851), and IR + FMC + αPD-1 and IR + FMC group (R2X = 0.704, R2Y = 0.798, and Q2 = 0.555). (D−F) Heat map of significantly changed metabolites in the comparison of FM and control group, IR + FMC and control group, and IR + FMC + αPD-1 and IR + FMC group. (G) Venn diagram of the differential metabolites.

representative for pathological analysis in the IR + FMC + αPD-1 group. The average body weights of the mice in each group show no significant reduction across all groups, as given in Figure S9D, indicating the good safety of these therapeutic interventions.

Meanwhile, the tumor-bearing mice were monitored until the tumor size reached 1500 mm^3 or the experimental end

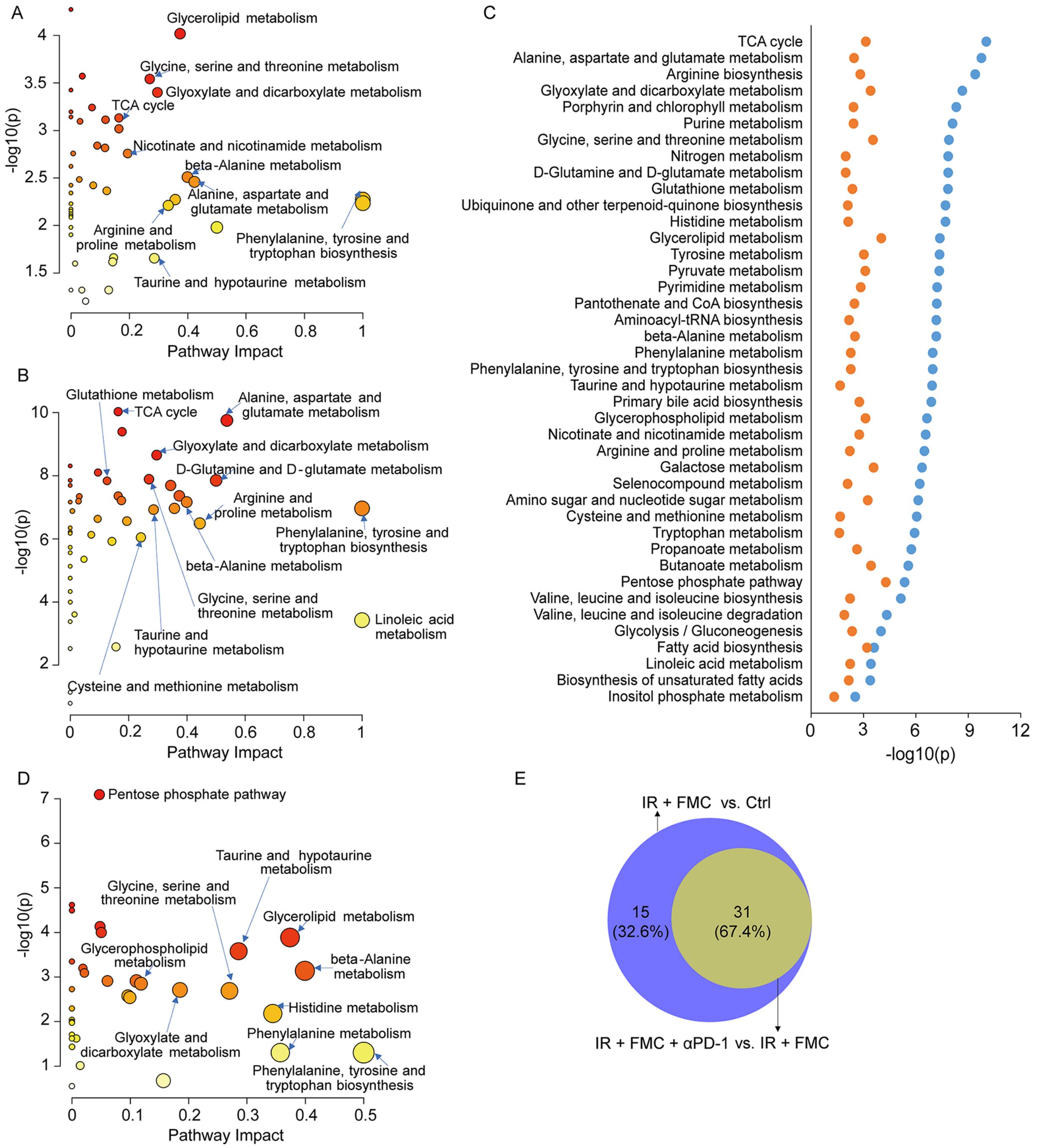

Figure 8. Disturbed pathways of the treated tumor. (A, B) Significantly changed pathways in the comparison of FM and control group and IR + FMC and control group. (C) *P* value distribution of shared significantly changed pathways in the comparison of FM and control group and IR + FMC and control group. (D) Significantly changed pathways in the comparison of IR + FMC + αPD-1 and IR + FMC group. (E) Venn diagram of significantly changed pathways in the comparison of IR + FMC and control group and IR + FMC and IR + FMC + αPD-1 group.

point was reached. Then, the mice were euthanized to analyze the level of lung metastasis. Figures 6F and S10A show the lung tissues from the control, IR + FMC, and IR + FMC + αPD-1 groups. It is evident that the control group exhibits numerous tumor nodules in the lung, whereas fewer metastatic tumor nodules can be observed in the lungs from the IR + FMC group and the IR + FMC + αPD-1 group, which are strongly supported by the statistical analysis of metastatic nodules in Figure S10B. Notably, IR + FMC group and IR + FMC + αPD-1 group display clear alveolar networks without significant tumor metastasis. These evidence suggest that FMC-based ISV can improve the tumor immunotherapy and inhibit the distant tumor growth and lung metastasis, owing to the enhancement of tumor cross-antigen presentation and systemic antitumor immune responses.

To further validate the systemic antitumor immune response induced by ISV, we examined the antigen-specific antibody response using an enzyme-linked immunosorbent assay kit. Specifically, two subtypes of IgG antibodies, i.e., IgG1 and IgG2α in mouse serum, were measured. As shown in Figure S10C, the IR + FMC group exhibited a 1-fold increase in the level of IgG1 compared to the control group. Furthermore, the combination of αPD-1 and IR + FMC resulted in even higher levels of IgG1 antibodies. The pattern of IgG2α antibody levels followed a similar trend, as shown in Figure S10D. These results confirmed that IR + FMC treatment can activate a systemic antigen-specific immune response, leading to the inhibition of the distant tumor growth and lung metastasis, which can be further enhanced by PD-1 blockade therapy. In addition, to assess the safety profile of FMC-based ISV, H&E staining on major organs was conducted, including the heart, liver, spleen, and kidney, at the experimental end point. Figure S11A presented the H&E staining results that indicated the absence of distinct inflammatory cell infiltration or damage in these organs, demonstrating the favorable biosafety of FMC-based ISV in vivo.

Mechanism of FMC-Based ISV for Inhibiting the Tumor Growth. Nontargeted metabolomic analysis was performed to investigate the mechanism behind the significant antitumor effects and abscopal effects of ISV in vivo. Tumor samples were collected from the treated and distant tumors of mice in four different groups, i.e., the IR + FMC + αPD-1 group, IR + FMC group, FM group, and control group. Metabolomic data were evaluated by using the quality control (QC) samples. As displayed in Figure S12A,B, the QC samples clustered in the score plots of the principal component analysis (PCA), and 94.6% of metabolic features had relative standard deviation (RSD) values below 30% in QC samples, indicating that the data were reliable.

A robust partial least-squares-discriminant analysis (PLS-DA) was first performed to gain a comprehensive understanding on the global metabolic changes in treated tumors. The results given in Figures 7A−C and S13A−C clearly demonstrate that significant shifts take place in metabolic profile of both FM and IR + FMC groups in comparison to those from the control group. Additionally, notable changes can also be observed if comparing the IR + FMC + αPD-1 group with the IR + FMC group. Through nonparametric tests, it was found that a total of 72, 95, and 42 identified metabolites exhibited significant differences between the following group pairs, i.e., FM group vs control group, IR + FMC group vs control group, and IR + FMC group vs IR + FMC + αPD-1 group, respectively (Table S1). These variations in these metabolites are presented in Figure 7D−F. It can be seen that 68 metabolites display significant changes when comparing FM and IR + FMC groups with the control group (Figure 7G). Most of these metabolites show increased levels after treatment, except for citrate that presents a decreased level. Notable examples of the affected metabolite classes include amino acids (glycine, serine, tryptophan, alanine, asparagine, etc.), organic acids (lactate, fumarate, glycerate, 2-hydroxyglutarate, etc.), fatty acids (palmitoleate, linoleate, oleate, etc.), and nucleosides (uracil, uridine 5-phosphate, etc.).

To investigate the potential mechanisms underlying the therapeutic effects of different treatments, the metabolites altered with reference to those of the control group were subjected to the pathway analysis using Metabo Analyst. The results given in Figure 8A,B reveal those significant disturbances in 45 pathways of the FM group and 46 pathways of the IR + FMC group. Among these pathways, 41 overlapping pathways depicted in Figure 8C are associated with energy, lipid, amino acid, and nucleotide metabolism, suggesting that substantial metabolic changes are induced by FM treatment and further amplified by IR + FMC treatment. Importantly, these changes in metabolic pathways are consistent with the variations of tumor volume and therapeutic outcomes upon different treatments. In comparison to the control group, there is a noticeable increase in glycolytic metabolites, such as glucose, D-glucose 6-phosphate, D-fructose 6-phosphate, and lactate, in the IR + FMC group. Additionally, tricarboxylic acid (TCA) cycle-related metabolites, including fumarate, malate, and 2-hydroxyglutarate, are upregulated, while citrate is downregulated. Disruptions of glycolysis and the TCA cycle represent tumor metabolic vulnerabilities that have garnered significant attention in therapeutic intervention research.[41] Their dysregulation observed in the IR + FMC group was linked to tumor remission induced by the treatment. Furthermore, the levels of lipid species such as octanoate, myristate, palmitoleate, and others are also found to increase in the IR + FMC group. Interestingly, the ratio of palmitate/linoleate, an indicator of de novo lipogenesis activity,[42] is significantly downregulated. These findings suggest that lipogenesis is attenuated while fatty acid oxidation (FAO) is enhanced upon IR + FMC treatment. It was reported that inhibition of lipogenesis positively contributed to tumor therapy.[43] Consistently, the product of the oxidation of fatty acid, 3-hydroxybutyrate, the ketone body with the highest content, and closely related to tumor suppression[44] is significantly upregulated in the IR + FMC group in comparison with the control group. In consequence of IR + FMC treatment, the elevation of polyunsaturated fatty acids that are highly susceptible to peroxidation,[45] along with the accumulation of ROS derived from FAO and IR and the increased cellular iron level introduced by FMC collectively stimulate tumor cell death through ferroptosis, which is supported by the facts that amino acids associated with ferroptosis exhibit significant increases in the IR + FMC group if compared to the control group. The increased levels of glutathione synthetic substrates including cysteine, glutamate, and glycine in the IR + FMC group indicate an enhanced demand for glutathione, which is likely attributed to high levels of ROS that triggers ferroptosis. Moreover, a substantial increase in glutamine in IR + FMC group can induce ferroptosis via glutaminolysis.[46] In consequence of IR + FMC + αPD-1 combined therapy, 31 significant pathways were found overlapped with those induced by IR + FMC (Figure 8D,E). Among the shared pathways, the pentose phosphate pathway, taurine and hypotaurine metabolism, glycerolipid metabolism, and β-alanine metabolism are involved. Especially, the upregulated glucose level significantly indicates further exacerbation of energy metabolism disorder, while the elevated expression of hypotaurine that serves as a precursor for taurine can enhance the function of CD8$^+$ T cells and promote the antitumor effects of αPD-1 antibody.[47] These evidence suggests that the perturbation of energy metabolism and the activation of taurine and hypotaurine metabolism collectively contribute to the augmented antitumor efficacy of FMC-based ISV/αPD-1 combined therapy. Furthermore, the serine level is significantly downregulated following IR + FMC + αPD-1 treatment. Serine metabolism is highly active in tumor cells, providing a rich source of one-carbon units for aberrant biosynthesis, maintaining redox homeostasis, promoting tumor progression, and exerting immunosuppressive effects.[48] The downregulation of serine metabolism observed in this study is undoubtedly beneficial for enhancing the immune response of T cells.

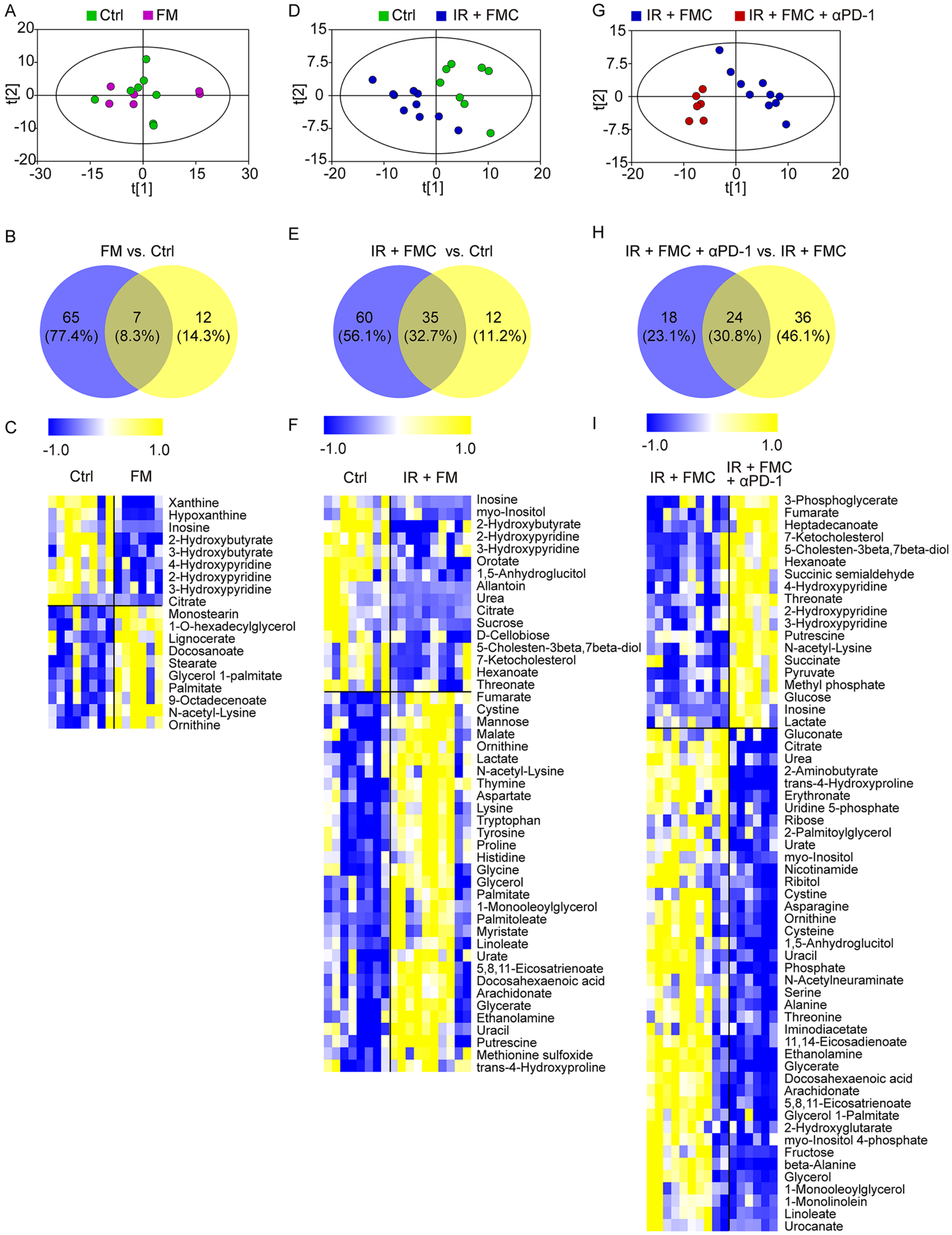

Figure 9. Metabolic profiles of the distant tumor. (A) PCA score plot of FM and control group (R2X = 0.758 and Q2 = 0.498). (B) Venn diagram of the differential metabolites in treated and distant tumor in the comparison of FM and control group. (C) Heat map of significantly changed metabolites in the comparison of FM and control group. (D) PLS-DA score plot of IR + FMC and Ctrl group (R2X = 0.653, R2Y = 0.783, and Q2 = 0.637). (E) Venn diagram of the differential metabolites in treated and distant tumor in the comparison of IR + FMC and Ctrl group. (F) Heat map of significantly changed metabolites in the comparison of IR + FMC and Ctrl group. (G) PLS-DA score plot of IR + FMC + αPD-1 and IR + FMC group (R2X = 0.71, R2Y = 0.914, and Q2 = 0.872). (H) Venn diagram of the differential metabolites in treated and distant tumor in the comparison of IR + FMC + αPD-1 and IR + FMC group. (I) Heat map of significantly changed metabolites in the comparison of IR + FMC + αPD-1 and IR + FMC group.

To further explore the mechanisms behind the abscopal antitumor effect of ISV in vivo, the metabolic profiles of distant tumors were further analyzed. Little variation can be observed from the global metabolic profiles of the distant tumors of mice treated with FM compared to its control (Figure 9A). However, further univariate analysis reveals that 19 metabolites exhibit significant differences and 7 metabolites are shared by the treated tumor and distant tumor from the FM group compared to the control group, as shown in Figure 9B and Table S1. Pathway analysis demonstrates that 11 pathways are notably altered in the distant tumors of mice treated with FM, as shown in Figures 9C and S14A,B. These variations are consistent with those observed in the treated tumor, involving alterations in glutathione metabolism, fatty acid metabolism, and purine metabolism, suggesting that these metabolic changes are somehow associated with the slight abscopal antitumor effect of FM.

To assess the impact of IR + FMC treatment on distant tumors, a supervised partial least-squares discriminant analysis (PLS-DA) model was adopted to analyze the results. Permutation tests were conducted to confirm that there was no overfitting. As shown in Figures 9D and S15A, distinct metabolic profiles are evident in the distant tumors of IR + FMC group compared to the control group. Specifically, 35 out of 47 identified differential metabolites are found to be common between the treated and distant tumors in the IR + FMC group when compared to the control group. Furthermore, the majority of these metabolites exhibit increased levels after the treatment (Figure 9E,F and Table S1). Based on these alterations, 41 significantly modulated pathways are discovered. Among them, 36 pathways exhibit notable changes in both treated and distant metastatic tumors following IR + FMC treatment. These pathways encompass crucial processes such as glycolysis, TCA cycle, glutathione metabolism, lipid metabolism, and tryptophan metabolism, as shown in Figure S15B,C. These pathways play a role in diverse cellular processes, including energy metabolism, regulation of ROS, ferroptosis, and immune responses. The modulations of these pathways therefore explain the abscopal antitumor effect of IR + FMC treatment.

In addition, a PLS-DA model was adopted to analyze the metabolic profile of the distant tumor for showing the difference between IR + FMC + αPD-1 and IR + FMC groups (Figures 9G and S15D). Through univariate analysis, 60 metabolites exhibiting notable difference between these two groups were identified. Among them, 24 metabolites are shared by the treated and distant tumors, including glucose, serine, inosine, and glycerol 1-palmitate (Figure 9H,I and Table S1). Moreover, 34 significantly altered pathways specifically in the distant tumor can be identified, with 23 of them being overlapped if comparing the results of the distant tumor before and after the treatment. These shared pathways include glycolysis, taurine and hypotaurine metabolism, and purine and pyrimidine metabolism (Figure S15E,F). Notably, the TCA cycle, pyruvate metabolism, and linoleic acid metabolism exhibit substantial disturbances in the distant tumors. Glycolytic metabolites such as 3-phosphoglycerate, pyruvate, and lactate, are found to notably be elevated in the distant tumor after treatment, apart from the upregulation of glucose. On the other hand, TCA cycle-related metabolites like citrate, succinate, and fumarate are exclusively altered in the distant tumor post-treatment. These findings indicate that the energy metabolism is not only perturbed, but also disrupted more heavily in the distant tumor than in the treated tumor if comparing IR + FMC + αPD-1 treatment with IR + FMC treatment. Moreover, apart from the reduction in lipid species such as glycerol 1-palmitate, 2-palmitoylglycerol, and 11,14-eicosadienoate, long-chain fatty acids such as arachidonate, linoleate, and docosahexaenoic acid are also found decreased, while the short-chain fatty acid hexanoate is found to accumulate exclusively in the distant tumors of IR + FMC + αPD-1 group when compared to the IR + FMC group, suggesting that derangement of lipid metabolism gets exacerbated in the distant tumors of IR + FMC + αPD-1 group.

STUDY LIMITATIONS

ISV is indeed an exciting area of research with potential for universal tumor therapy. However, this study underlines a significant challenge, the intricate balance between antigen production and T cell exhaustion. Effectively managing this delicate equilibrium is crucial to optimize the therapeutic outcomes of ISV. Furthermore, an essential aspect to be tackled in ISV is the visualization of antigen production and presentation. The ability to visualize these processes holds immense potential for a deeper understanding of immune response dynamics and facilitates the refinement of ISV strategies. By addressing these critical challenges, we can propel the advancement of ISV and unlock its full potential in realizing universal tumor therapy.

CONCLUSIONS

In summary, we have developed a biocompatible FMC nanoadjuvant capable of capturing tumor antigens to form FMC-based ISV upon IR. By strategically designing and optimizing nanoadjuvant, it is possible to create an environment that promotes robust immune activation and overcomes the immunosuppressive barriers encountered in poorly immunogenic tumors. It has been demonstrated that the resulting ISV has the ability to activate antigen-presenting DCs, expand CD8$^+$ cytotoxic T cells, and reduce the population of suppressive immune cells. These findings highlight the potential of FMC-based ISV combined with PD-1 blockade therapy for effectively reversing T cell exhaustion, activating antitumor immunity, and improving the therapeutic outcomes in cancer treatment, which well addresses the challenges related to low immunogenicity and insufficient antigen presentation. Further understanding of the underlying mechanisms and metabolomic alterations can guide the development of immunotherapeutic strategies.

METHODS

Materials. Cyclohexane, acetone, tetrahydrofuran (THF), acetic acid, sodium acetate, concentrated hydrochloric acid, hydroxylamine hydrochloride, 1,10-phenanthroline monohydrate, glycine, and SDS were purchased from Sinopharm Chemical Reagent Co., Ltd. Cy5.5-CpG, CpG, Tris, glycerin, bromophenol blue, and DTT were purchased from Bioengineering Co., Ltd. Interleukin 4 (IL-4) and granulocyte-macrophage colony-stimulating factor (GM-CSF) were purchased from Pepro Tech. In vivo Mab antimouse PD-1 was purchased from Bio X Cell. Mal-PEG-Dp was purchased from Suzhou Xinying Biomedical Technology Co., Ltd. Antimouse CD11c (BV421), CD86 (PerCP-Cy5.5), MHC II (FITC), PD-1 (BV421), CD3 (PE), and CD4 (BV421) were purchased from BioLegend. Antimouse CD80 (PE) and CD4 (APC) were purchased from BD Biosciences. Antimouse CD103 (PE-Cy7), CD3 (FITC), CD8 (PerCP-Cy5.5), and IFN-γ (FITC) were purchased from Elabscience.

Antimouse OX40 (PE), CD25 (APC), and Foxp3 (PE) were purchased from eBioscience.

Cell Lines and Animals. All cell lines were acquired from the Institute of Biochemical Cells, Chinese Academy of Sciences. The cell lines were cultured according to the instructions provided by the vendor.

All animal experiments were conducted under approval from the Animal Ethics Committee of Soochow University (SYXK2021-0065). The experiments were also conducted in compliance with a protocol approved by the institutional animal care and use committee. The experimental animals were sourced from the Experimental Animals Center of Soochow University.

Tumor Models. Female BALB/c mice were subcutaneously inoculated with 4×10^5 of 4T1-Luc breast tumor cells. To monitor tumor growth, the sizes of the tumors were measured every other day using a caliper. Tumor volume was calculated using the following formula: tumor volume = length × width^2/2. Additionally, mouse tumor growth was monitored through bioluminescence imaging using an IVIS Spectrum Imaging System (PerkinElmer). For this purpose, luciferin (1 mg/mL) was intramuscularly injected into the mice.

At the ethical end point, when the tumor volume reached 1500 mm^3, the mice were euthanized. It is important to note that all animal experiments were conducted under anesthesia using 2.5% isoflurane.

Preparation of the FMC. Typically, 2 mL of an oil-phase Fe_3O_4 solution (8.86 mg/mL) was added to 30 mL of acetone. The mixture was then subjected to centrifugation at 5000 rpm for 7 min to remove the supernatant. Subsequently, 2 mL of tetrahydrofuran was added to dissolve the precipitate under oscillation.

Next, 177.2 mg of PEG2000-Mal (mass ratio, Fe:PEG-Mal = 1:10) was weighed, and 2 mL of THF was added to completely dissolve it. The Fe_3O_4 solution in tetrahydrofuran was combined with the PEG-Mal solution, followed by thorough mixing and ultrasonication for 1−2 h. The resulting mixture was then cooled to room temperature, and cyclohexane with 10 times the volume of reaction mixture was added. After centrifugation at 8000 rpm for 10 min, the supernatant was removed and the precipitate was obtained and dried.

To dissolve the obtained precipitate, 2 mL of ultrapure water was added. The solution was subsequently subjected to centrifugation at 10000 rpm for 6 min, followed by filtration using a 0.22 μm filter membrane. This ultrafiltration process was repeated 3−4 times to eliminate excess PEG ligand. Finally, the aqueous FM solution was acquired and stored at 4 °C for future use.

For the next step, 40 μL of the FM solution was added to 200 μL of CpG and the mixture stirred at room temperature for approximately 9 h. The resulting solution was then centrifuged at 4000 rpm for 5 min, followed by 2−3 rounds of ultrafiltration. The final product obtained was stored at 4 °C for later use. The concentration of Fe ions in the solution was determined by using the phenanthroline method.

CpG Loading. A solution of Cy5.5-labeled CpG (100 μM) was prepared in PBS and subsequently diluted into solutions with a series of concentrations, i.e., 0.3, 0.7, 0.8, 1, 2, 2.7, and 4 μM, using PBS. The absorbance of each Cy5.5-labeled CpG solution at 690 nm was measured using a UV−vis spectrophotometer. By plotting the absorbance values against the corresponding concentrations, a standard curve for Cy5.5-labeled CpG was obtained.

Following the aforementioned approaches, FMC$^{Cy5.5}$ was prepared. The loading efficiency of Cy5.5-labeled CpG in FMC$^{Cy5.5}$ was determined through UV−vis absorption spectroscopy.

Characterization. The morphology of the FMC nanoparticles (NPs) was characterized by using a transmission electron microscope (Tecnai G2 spirit BioTwin, FEI). The hydrodynamic size and ζ potential of the NPs were determined by using dynamic light scattering (DLS) with a Zetasizer ZS90 instrument from Malvern. The absorbance spectra of the NPs were recorded by using a UV−vis−near-IR (NIR) spectrophotometer (Lambda 35, PerkinElmer). For NIR fluorescence imaging, an IVIS Spectrum system from PerkinElmer was utilized. Flow cytometric analysis was conducted using a BD Biosciences FACSCalibur flow cytometer.

Antigen Capturing In Vitro. 4T1-Luc tumor cells were seeded into cell culture dishes and incubated in RPMI-1640 medium supplemented with 10% FBS and 1% penicillin−streptomycin. The cells were then cultured at 37 °C under 5% CO_2 for 24 h. Subsequently, the cells were washed three times with PBS and subjected to photon radiation at a dose of 20 Gy by using an X-RAD 320ix machine operating at a peak voltage of 320 kV and 11 mA.

Irradiated and unirradiated 4T1-Luc cells were incubated in PBS for 30 min. Subsequently, the supernatant was collected and centrifuged at 4000 rpm for 10 min to remove any insoluble cellular debris. The sulfhydryl content in the resulting supernatant was assessed using an ELLMAN agent, 5,5′-dithiobis-2-nitrobenzoic acid (DTNB).

Thereafter, FMC particles were mixed with antigen-containing supernatants derived from the irradiated 4T1-Luc cells following the aforementioned protocol. The mixture was incubated at 37 °C for 4 h. After the incubation period, the FMC particles were washed with PBS using ultrafiltration with an Amicon Ultra system equipped with an Ultracel membrane having a nominal molecular weight limit (NMWL) of 100000.

To determine the concentration of the antigen captured by the FMC NPs, the bicinchoninic acid (BCA) protein concentration assay was employed. The same procedures mentioned above were taken to investigate the antigen-capturing ability of FMC NPs for different types of tumor cells, including gastric tumors (803 cells), colon tumors (MC38 cells), melanoma (B16F10 cells), melanoma with high OVA expression (B16F10-OVA cells), leukemia cells (L1210 cells), etc.

Analysis of Proteins Captured by FMC NPs. Briefly, 100 μL of SDS sample buffer was added into the solution of antigen-captured nanoparticles, elution of the above proteins was performed, and the mixture was incubated at 95 °C for 10 min. The solution was then centrifuged at 8000 rpm for 15 min, and the eluted protein supernatant was transferred to a new EP tube. The concentration of the supernatant protein was determined by the BCA method. After 20 μL of eluted proteins was loaded into a 12% (w/v) SDS gel, the electrophoresis was run at room temperature under 120 V for 1−2 h. In detail, the SDS gel was incubated in an Instant Blue staining solution for at least 15 min. The protein bands were then rinsed and soaked in ultrapure water until they were clearly visible. Subsequently, the protein bands were enzymatically hydrolyzed;[49] the peptide segments were desalted, isolated, and identified by capillary liquid chromatography tandem mass spectrometry (LC-MS/MS).

BMDCs Incubated with FMC-Based ISV In Vitro. For in vitro BMDC activation studies, C57BL/6J mice aged 6−8 weeks were sacrificed, and BMDCs were isolated from the tibiae and femurs and cultured in the presence of GM-CSF and IL-4 (20 ng/μL) using 4T1-Luc cell growth medium described previously.

On the third and fifth days of culture, the supernatant was discarded and fresh medium was added to sustain the culture. The BMDCs were counted and seeded into confocal dishes at a density of 1×10^5 cells per dish. Once the cells adhered to the dish surface, the culture medium was aspirated and 1 mL of medium containing TAA-loaded FMC$^{Cy5.5}$ was added. The culture was continued for 24 h.

After the incubation period, the culture medium was removed and the BMDCs were stained using LysoTracker to label lysosomes and Hoechst 33342 to stain the nuclei. Following completion of the staining procedure, the cells were imaged and examined by using laser confocal microscopy.

MRI Studies of FMC in Simulated Lysosomal Fluids In Vitro. FMC solutions with different concentrations at pH 7.4, i.e., 0, 0.1, 0.2, 0.3, 0.4, and 0.5 mM, were prepared. In parallel, FMC solutions with the same concentrations mentioned above but in an acetic acid−sodium acetate buffer at pH 5.5 were also prepared. Subsequently, H_2O_2 was added to each solution, to dilute the solution to a final concentration of 100 μM. After incubation at room temperature for 10 min, MRI was conducted to investigate the variation induced by the incubation media.

Activation of BMDC In Vitro. On the seventh day of culture, BMDCs were incubated with various agents, including CpG, FM, FMC, TAA-loaded FM, TAA-loaded FMC, and 4T1-Luc tumor-associated antigens, respectively, for 24 h.

After the incubation, the BMDCs were stained using antimouse CD11c-PE, antimouse CD80-FITC, antimouse CD86-PerCP-Cy5.5, and antimouse CD103-PE/Cy7 antibodies. Subsequently, flow cytometry analysis was performed to evaluate the expression levels of these markers on the BMDCs and assess their activation status.

MRI and Fluorescence Imaging of FMC In Vivo. To perform MRI imaging, 4 × 10^5 4T1-Luc breast tumor cells were subcutaneously inoculated into the right flank of female BALB/c mice. Once the tumors reached a volume of 200 mm^3, the mice were randomly divided into 2 groups that received treatment with FMC or IR + FMC. MRI imaging was performed at different time points after intratumoral injection of FMC (25 μL, 0.2 mg/mL Fe), i.e., 0.5, 1, 2, 4, 6, 8, 10, and 24 h, for comparison with that recorded pre-injection.

For fluorescence imaging, 4T1-Luc mice were also randomly divided into 3 groups receiving treatments with IR + $CpG^{Cy5.5}$, $FMC^{Cy5.5}$, or IR + $FMC^{Cy5.5}$. Fluorescence imaging was performed at different time points after intratumoral injection of FMC (25 μL, 17 μM CpG), i.e., 0.5, 2, 8, and 24 h and 5 days, for comparison with that recorded preinjection.

Labeling αPD-1 with Cy5. In brief, the αPD-1 antibody was mixed with 2-iminothioane hydrochloride in PBS by a molar ratio of 1:10. After the reaction was performed at room temperature for 1 h, excessive sulfonyl-Cy5-E maleimide was introduced. The reaction mixture was stirred at room temperature for 2 h. Then, the Cy5-labeled antibody was purified and concentrated using an Amicon Ultra15 device with a molecular weight cutoff (MWCO) of 10 kDa from Millipore. The concentration of conjugated αPD-1 antibodies was determined by using a BCA protein assay kit.

PD-1 Targeted Imaging In Vivo. To validate the effects of PD-1 elevation on $CD8^+$ T cells in tumor tissues, model mice with breast tumors were intravenously injected with 200 μL of αPD-1-Cy5 solution at a dose of 10 mg kg^{-1}. Subsequently, IVIS imaging was conducted at 1 and 30 min and 1, 2, 4, 6, 8, 10, 12, 24, 48, 72, 96, and 120 h postinjection to monitor and assess the distribution and localization of αPD-1-Cy5 within the tumor tissue over time.

Antitumor Effects of ISV in Combination with αPD-1 In Vivo. Female BALB/c mice were subcutaneously transplanted with 4 × 10^5 4T1-Luc breast tumor cells in the right flank. When the tumor volume reached approximately 100 mm^3, the mice were randomly divided into 8 groups, i.e., (1) control, (2) CpG, (3) FMC, (4) TAA-loaded FM, (5) IR, (6) IR + CpG, (7) IR + FM, and (8) IR + TAA-loaded FMC.

On the first and second days of the treatment, the tumors were subjected to local irradiation with a single dose of 6 Gy at a rate of 1 Gy/min, with the rest of the mouse body being shielded with a lead plate to minimize the unwanted radiation exposure. After the radiotherapy session, the mice received three rounds of intratumoral injections of different therapeutic agents every 2 days. Throughout the treatment, tumor growth and the mice's body weight were monitored every 2 days to assess the therapeutic effects. On the eighth day of treatment, all mice were sacrificed and their tumor tissues were analyzed using flow cytometry to investigate the immune response elicited by the treatment.

Flow Cytometric Analysis. Flow cytometry was employed to characterize the tumor microenvironment using single-cell suspensions prepared by enzymatic digestion of tumors, spleens, and tumor-draining lymph nodes, respectively. The tissues were digested to cell suspension with 1 mg/mL collagenase IV (Sigma-Aldrich) and 0.02 mg/mL DNaseI (Sigma-Aldrich) for 1 h at 37 °C and then were passed through a 70 μm cell strainer to remove undigested tissues. To eliminate the red blood cells (RBCs), RBC lysate from Beyotime was added and the mixture incubated for 5 min. PBS was added to wash the single-cell solution 3 times for cleaning. Dendritic cells in the draining lymph nodes were stained using anti-CD11c-BV421, anti-CD80-PE, anti-CD86-PerCP-Cy5.5, anti-MHC II-FITC, and anti-CD103-PE-Cy7 antibodies, respectively. T cells in tumors were stained using anti-CD3-FITC, anti-CD8-PerCP-Cy5.5, anti-CD4-APC, anti-OX40-PE, anti-PD-1-BV421, anti-IFN-γ-FITC, anti-CD25-APC, and anti-Foxp3-PE antibodies, respectively. An intracellular staining kit (BD) was used to stain Foxp3 and IFN-γ according to the manufacturer's instructions. After staining, cells were washed twice with PBS and suspended in PBS at 4 °C prior to analysis. Flow cytometry data were acquired using a BD FACS Verse flow cytometer and analyzed using FlowJo software (Treestar).

Serum ELISA Analysis. Mouse serum was isolated from whole blood after eye orbit blood collection and coagulated at room temperature for 40 min. Samples were centrifuged at 4000 rpm for 10 min, and serum supernatant was collected. Then, the serum levels of IgG subclasses IgG1 and IgG2α in mice were quantitatively determined with IgG1 and IgG2α Mouse ELISA Kits (Multi Sciences). First, the microporous plate was precoated with antibodies for 30 s, and then, prediluted serum supernatant was added to detect antibodies. After incubation at room temperature for 3 h, the microwell plates were cleaned with ultrapure water 6 times. The chromogenic agent was added to the microplate and incubated at room temperature for 10 min in the dark, followed by termination of the solution for 20 min to stop the reaction. The absorbance value of the sample at 450 nm was detected by a UV−vis−NIR spectrophotometer, and the concentrations were calculated according to the manufacturer's instructions.

Nontargeted Metabolomics Analysis. The nontargeted metabolomic analysis was conducted following a previously established protocol.[50] Each tumor had two copies, except the distant tumor of the IR + FMC + αPD-1 group had six copies and weighed approximately 15 mg. Tumor homogenization and metabolite extraction were performed using a grinding apparatus (MM-400 Retsch Technology, Haan, Germany) with a methanol−water solvent (4:1, v/v). To facilitate the analysis, an internal standard (tridecanoic acid) at a concentration of 2.5 μg/mL was included in the solvent. After homogenization, the supernatant was collected and subjected to lyophilization. The resulting dried sample was then oximated and silylated prior to GC-MS analysis. Quality control (QC) samples were prepared using the remaining supernatant and underwent the same pretreatment steps as the actual samples.

Metabolic profiling was carried out using a GCMS-QP2010 plus system (Shimadzu, Kyoto, Japan) coupled with a DB-5 MS fused-silica capillary column (30 m × 0.25 mm × 0.25 μm, Agilent Technologies, Palo Alto, CA, USA). The acquired data were subsequently processed using ChromTOF 4.43 software (LECO, St. Joseph, MI, USA) for qualitative analysis and GC-MS browser software (Shimadzu, Kyoto, Japan) for quantitative analysis. The intensity of metabolic features was normalized according to the internal standard's intensity and adjusted based on the tumor weight.

Multivariate analysis was performed using SIMCA 14.1 software (Umetrics, Umea, Sweden), while univariate analysis was conducted using SPSS 18.0 software. These analyses aimed to identify significant metabolic differences among the experimental groups.

Statistical Analysis. All measurements were performed on 3 or more independent replicates from distinct samples. GraphPad Prism v7.0d was used to perform statistical analysis. All results are presented as the mean ± standard error. Kaplan−Meier survival curves were analyzed using the log-rank Mantel−Cox test, and column statistics were analyzed using Student's *t* test. * Indicates significance at $p < 0.05$, ** indicates significance at $p < 0.01$, *** indicates significance at $p < 0.001$, and **** indicates significance at $p < 0.0001$.

ASSOCIATED CONTENT

Supporting Information

The Supporting Information is available free of charge at https://pubs.acs.org/doi/10.1021/acsnano.3c10225.

Characterization of FMC and ISV after antigen capture, uptake of materials by BMDC, in vitro imaging data, partial data on immune activation, analysis of αPD-1-Cy5, imaging of mice tumors, tumor volume curves, body weight curves, survival curves, H&E staining of lung, serum cytokine detection results, H&E staining of major organs, metabolomics quality control, and specific differential metabolites (PDF)

AUTHOR INFORMATION

Corresponding Authors

Yang Zhou − *Ningbo Institute of Innovation for Combined Medicine and Engineering, The Affiliated Li Huili Hospital, Ningbo University, Ningbo 315201, China*; Email: zhouyang610@163.com

Yong Wang − *State Key Laboratory of Radiation Medicine and Protection, School for Radiological and Interdisciplinary Sciences (RAD-X), Soochow University, Collaborative Innovation Center of Radiation Medicine of Jiangsu Higher Education Institutions, Soochow University, Suzhou 215123, China*; orcid.org/0000-0003-4061-7956; Email: yongwang@suda.edu.cn

Mingyuan Gao − *State Key Laboratory of Radiation Medicine and Protection, School for Radiological and Interdisciplinary Sciences (RAD-X), Soochow University, Collaborative Innovation Center of Radiation Medicine of Jiangsu Higher Education Institutions, Soochow University, Suzhou 215123, China; The Second Affiliated Hospital of Soochow University, Soochow University, Suzhou 215004, China*; orcid.org/0000-0002-7360-3684; Email: gaomy@suda.edu.cn

Authors

Pei Xu − *Ningbo Institute of Innovation for Combined Medicine and Engineering, The Affiliated Li Huili Hospital, Ningbo University, Ningbo 315201, China; State Key Laboratory of Radiation Medicine and Protection, School for Radiological and Interdisciplinary Sciences (RAD-X), Soochow University, Collaborative Innovation Center of Radiation Medicine of Jiangsu Higher Education Institutions, Soochow University, Suzhou 215123, China*

Jie Ma − *State Key Laboratory of Radiation Medicine and Protection, School for Radiological and Interdisciplinary Sciences (RAD-X), Soochow University, Collaborative Innovation Center of Radiation Medicine of Jiangsu Higher Education Institutions, Soochow University, Suzhou 215123, China*

Yuan Gu − *State Key Laboratory of Radiation Medicine and Protection, School for Radiological and Interdisciplinary Sciences (RAD-X), Soochow University, Collaborative Innovation Center of Radiation Medicine of Jiangsu Higher Education Institutions, Soochow University, Suzhou 215123, China*

Xiaju Cheng − *State Key Laboratory of Radiation Medicine and Protection, School for Radiological and Interdisciplinary Sciences (RAD-X), Soochow University, Collaborative Innovation Center of Radiation Medicine of Jiangsu Higher Education Institutions, Soochow University, Suzhou 215123, China*

Yangyun Wang − *State Key Laboratory of Radiation Medicine and Protection, School for Radiological and Interdisciplinary Sciences (RAD-X), Soochow University, Collaborative Innovation Center of Radiation Medicine of Jiangsu Higher Education Institutions, Soochow University, Suzhou 215123, China*

Complete contact information is available at:
https://pubs.acs.org/10.1021/acsnano.3c10225

Author Contributions

[‖]P.X. and J.M. contributed equally to this work.

Notes

The authors declare no competing financial interest.

ACKNOWLEDGMENTS

This work was supported by the National Natural Science Foundation of China (22122407, 12075164, 12175162, 81972964, 82130059), the Science and Technology Project from Suzhou City (KJXW2022024), the Natural Science Foundation of Ningbo (2023J031), and the Tang Scholar Program, A Priority Academic Program Development of Jiangsu Higher Education Institutions (PAPD).

REFERENCES

(1) Topalian, S. L.; Taube, J. M.; Pardoll, D. M. Neoadjuvant checkpoint blockade for cancer immunotherapy. *Science* **2020**, *367* (6477), No. eaax0182.

(2) Yap, T. A.; Parkes, E. E.; Peng, W.; Moyers, J. T.; Curran, M. A.; Tawbi, H. A. Development of Immunotherapy Combination Strategies in Cancer. *Cancer Discovery* **2021**, *11* (6), 1368−1397.

(3) Vitale, I.; Shema, E.; Loi, S.; Galluzzi, L. Intratumoral heterogeneity in cancer progression and response to immunotherapy. *Nat. Med.* **2021**, *27* (2), 212−224.

(4) Lin, M. J.; Svensson-Arvelund, J.; Lubitz, G. S.; Marabelle, A.; Melero, I.; Brown, B. D.; Brody, J. D. Cancer vaccines: the next immunotherapy frontier. *Nat. Cancer* **2022**, *3* (8), 911−926.

(5) Demaria, O.; Cornen, S.; Daëron, M.; Morel, Y.; Medzhitov, R.; Vivier, E. Harnessing innate immunity in cancer therapy. *Nature* **2019**, *574* (7776), 45−56.

(6) Harari, A.; Graciotti, M.; Bassani-Sternberg, M.; Kandalaft, L. E. Antitumour dendritic cell vaccination in a priming and boosting approach. *Nat. Rev. Drug Discovery* **2020**, *19* (9), 635−652.

(7) Sellars, M. C.; Wu, C. J.; Fritsch, E. F. Cancer vaccines: Building a bridge over troubled waters. *Cell* **2022**, *185* (15), 2770−2788.

(8) Ott, P. A.; Wu, C. J. Cancer Vaccines: Steering T Cells Down the Right Path to Eradicate Tumors. *Cancer Discovery* **2019**, *9* (4), 476−481.

(9) Golden, E. B.; Marciscano, A. E.; Formenti, S. C. Radiation and In-Situ Tumor Vaccination. *Int. J. Radiation Oncol. Biol. Phys.* **2020**, *108* (4), 891−898.

(10) Melero, I.; Castanon, E.; Alvarez, M.; Champiat, S.; Marabelle, A. Intratumoural administration and tumour tissue targeting of cancer immunotherapies. *Nat. Rev. Clin. Oncol.* **2021**, *18* (9), 558−576.

(11) Saxena, M.; van der Burg, S. H.; Melief, C. J. M.; Bhardwaj, N. Therapeutic cancer vaccines. *Nat. Rev. Cancer* **2021**, *21* (6), 360−378.

(12) Zhu, J.; Ke, Y.; Liu, Q.; Yang, J.; Liu, F.; Xu, R.; Zhou, H.; Chen, A.; Xiao, J.; Meng, F.; Yu, L.; Li, R.; Wei, J.; Liu, B. Engineered Lactococcus lactis secreting Flt3L and OX40 ligand for in situ vaccination-based cancer immunotherapy. *Nat. Commun.* **2022**, *13* (1), 7466.

(13) Wang, Y.; Wu, Y.; Li, L.; Ma, C.; Zhang, S.; Lin, S.; Zhang, L. W.; Wang, Y.; Gao, M. Chemotherapy-Sensitized In Situ Vaccination for Malignant Osteosarcoma Enabled by Bioinspired Calcium Phosphonate Nanoagents. *ACS Nano* **2023**, *17* (7), 6247−6260.

(14) Gu, Y.; Lin, S.; Wu, Y.; Xu, P.; Zhu, W.; Wang, Y.; Cheng, X.; Zhang, L. W.; Stauber, R. H.; Wang, Y.; Gao, M. Targeting STING Activation by Antigen-Inspired MnO2 Nanovaccines Optimizes Tumor Radiotherapy. *Adv. Healthcare Mater.* **2023**, *12* (12), No. 2300028.

(15) Frank, M. J.; Reagan, P. M.; Bartlett, N. L.; Gordon, L. I.; Friedberg, J. W.; Czerwinski, D. K.; Long, S. R.; Hoppe, R. T.; Janssen, R.; Candia, A. F.; Coffman, R. L.; Levy, R. In Situ Vaccination with a TLR9 Agonist and Local Low-Dose Radiation Induces Systemic Responses in Untreated Indolent Lymphoma. *Cancer Discovery* **2018**, *8* (10), 1258−1269.

(16) Hammerich, L.; Marron, T. U.; Upadhyay, R.; Svensson-Arvelund, J.; Dhainaut, M.; Hussein, S.; Zhan, Y.; Ostrowski, D.; Yellin, M.; Marsh, H.; Salazar, A. M.; Rahman, A. H.; Brown, B. D.; Merad, M.; Brody, J. D. Systemic clinical tumor regressions and potentiation of PD1 blockade with in situ vaccination. *Nat. Med.* **2019**, *25* (5), 814−824.

(17) Roth, G. A.; Picece, V. C. T. M.; Ou, B. S.; Luo, W.; Pulendran, B.; Appel, E. A. Designing spatial and temporal control of vaccine responses. *Nat. Rev. Mater.* **2022**, *7* (3), 174−195.

(18) Yasmin-Karim, S.; Ziberi, B.; Wirtz, J.; Bih, N.; Moreau, M.; Guthier, R.; Ainsworth, V.; Hesser, J.; Makrigiorgos, G. M.; Chuong, M. D.; Wei, X.; Nguyen, P. L.; Ngwa, W. Boosting the Abscopal Effect Using Immunogenic Biomaterials With Varying Radiation Therapy Field Sizes. *Int. J. Radiation Oncol. Biol. Phys.* **2022**, *112* (2), 475−486.

(19) Atasheva, S.; Shayakhmetov, D. M. Oncolytic Viruses for Systemic Administration: Engineering a Whole Different Animal. *Mol. Ther.* **2021**, *29* (3), 904−907.

(20) Kepp, O.; Marabelle, A.; Zitvogel, L.; Kroemer, G. Oncolysis without viruses - inducing systemic anticancer immune responses with local therapies. *Nat. Rev. Clin. Oncol.* **2020**, *17* (1), 49−64.

(21) Scheetz, L.; Park, K. S.; Li, Q.; Lowenstein, P. R.; Castro, M. G.; Schwendeman, A.; Moon, J. J. Engineering patient-specific cancer immunotherapies. *Nat. Biomed. Eng.* **2019**, *3* (10), 768−782.

(22) Chen, J.; Qiu, M.; Ye, Z.; Nyalile, T.; Li, Y.; Glass, Z.; Zhao, X.; Yang, L.; Chen, J.; Xu, Q. In situ cancer vaccination using lipidoid nanoparticles. *Sci. Adv.* **2021**, *7* (19), No. eabf1244.

(23) Min, Y.; Roche, K. C.; Tian, S.; Eblan, M. J.; McKinnon, K. P.; Caster, J. M.; Chai, S.; Herring, L. E.; Zhang, L.; Zhang, T.; DeSimone, J. M.; Tepper, J. E.; Vincent, B. G.; Serody, J. S.; Wang, A. Z. Antigen-capturing nanoparticles improve the abscopal effect and cancer immunotherapy. *Nat. Nanotechnol.* **2017**, *12*, 877.

(24) Zhang, Y.; Sriramaneni, R. N.; Clark, P. A.; Jagodinsky, J. C.; Ye, M.; Jin, W.; Wang, Y.; Bates, A.; Kerr, C. P.; Le, T.; Allawi, R.; Wang, X.; Xie, R.; Havighurst, T. C.; Chakravarty, I.; Rakhmilevich, A. L.; O'Leary, K. A.; Schuler, L. A.; Sondel, P. M.; Kim, K.; Gong, S.; Morris, Z. S. Multifunctional nanoparticle potentiates the in situ vaccination effect of radiation therapy and enhances response to immune checkpoint blockade. *Nat. Commun.* **2022**, *13* (1), 4948.

(25) Li, J.; Xie, L.; Sang, W.; Li, W.; Wang, G.; Yan, J.; Zhang, Z.; Tian, H.; Fan, Q.; Dai, Y. A Metal-Phenolic Nanosensitizer Performs Hydrogen Sulfide-Reprogrammed Oxygen Metabolism for Cancer Radiotherapy Intensification and Immunogenicity. *Angew. Chem., Int. Ed.* **2022**, *61* (18), No. e202200830.

(26) Wang, G.; Li, B.; Tian, H.; Xie, L.; Yan, J.; Sang, W.; Li, J.; Zhang, Z.; Li, W.; Dai, Y. A Metal-Phenolic Nanocoordinator Launches Radiotherapeutic Cancer Pyroptosis Through an Epigenetic Mechanism. *Adv. Funct. Mater.* **2023**, *33* (23), No. 2213425.

(27) Rudqvist, N.-P.; Charpentier, M.; Lhuillier, C.; Wennerberg, E.; Spada, S.; Sheridan, C.; Zhou, X. K.; Zhang, T.; Formenti, S. C.; Sims, J. S.; Alonso, A.; Demaria, S. Immunotherapy targeting different immune compartments in combination with radiation therapy induces regression of resistant tumors. *Nat. Commun.* **2023**, *14* (1), 5146.

(28) Vodnala, S. K.; Eil, R.; Kishton, R. J.; Sukumar, M.; Yamamoto, T. N.; Ha, N.-H.; Lee, P.-H.; Shin, M.; Patel, S. J.; Yu, Z.; Palmer, D. C.; Kruhlak, M. J.; Liu, X.; Locasale, J. W.; Huang, J.; Roychoudhuri, R.; Finkel, T.; Klebanoff, C. A.; Restifo, N. P. T cell stemness and dysfunction in tumors are triggered by a common mechanism. *Science* **2019**, *363* (6434), No. eaau0135.

(29) Yu, Y.-R.; Imrichova, H.; Wang, H.; Chao, T.; Xiao, Z.; Gao, M.; Rincon-Restrepo, M.; Franco, F.; Genolet, R.; Cheng, W.-C.; Jandus, C.; Coukos, G.; Jiang, Y.-F.; Locasale, J. W.; Zippelius, A.; Liu, P.-S.; Tang, L.; Bock, C.; Vannini, N.; Ho, P.-C. Disturbed mitochondrial dynamics in CD8(+)TILs reinforce T cell exhaustion. *Nat. Immunol.* **2020**, *21* (12), 1540−1551.

(30) Kersten, K.; Hu, K. H.; Combes, A. J.; Samad, B.; Harwin, T.; Ray, A.; Rao, A. A.; Cai, E.; Marchuk, K.; Artichoker, J.; Courau, T.; Shi, Q.; Belk, J.; Satpathy, A. T.; Krummel, M. F. Spatiotemporal co-dependency between macrophages and exhausted CD8(+) T cells in cancer. *Cancer Cell* **2022**, *40* (6), 624−638 e9.

(31) Bassez, A.; Vos, H.; Van Dyck, L.; Floris, G.; Arijs, I.; Desmedt, C.; Boeckx, B.; Vanden Bempt, M.; Nevelsteen, I.; Lambein, K.; Punie, K.; Neven, P.; Garg, A. D.; Wildiers, H.; Qian, J.; Smeets, A.; Lambrechts, D. A single-cell map of intratumoral changes during anti-PD1 treatment of patients with breast cancer. *Nat. Med.* **2021**, *27* (5), 820−832.

(32) Zhang, Y.; Hu, J.; Ji, K.; Jiang, S.; Dong, Y.; Sun, L.; Wang, J.; Hu, G.; Chen, D.; Chen, K.; Tao, Z. CD39 inhibition and VISTA blockade may overcome radiotherapy resistance by targeting exhausted CD8+ T cells and immunosuppressive myeloid cells. *Cell Rep. Med.* **2023**, *4* (8), No. 101151.

(33) Khalil, D. N.; Suek, N.; Campesato, L. F.; Budhu, S.; Redmond, D.; Samstein, R. M.; Krishna, C.; Panageas, K. S.; Capanu, M.; Houghton, S.; Hirschhorn, D.; Zappasodi, R.; Giese, R.; Gasmi, B.; Schneider, M.; Gupta, A.; Harding, J. J.; Moral, J. A.; Balachandran, V. P.; Wolchok, J. D.; Merghoub, T. In situ vaccination with defined factors overcomes T cell exhaustion in distant tumors. *J. Clin. Invest.* **2019**, *129* (8), 3435−3447.

(34) Fitzgerald, K. A.; Kagan, J. C. Toll-like Receptors and the Control of Immunity. *Cell* **2020**, *180* (6), 1044−1066.

(35) Wculek, S. K.; Cueto, F. J.; Mujal, A. M.; Melero, I.; Krummel, M. F.; Sancho, D. Dendritic cells in cancer immunology and immunotherapy. *Nat. Rev. Immunol.* **2020**, *20* (1), 7−24.

(36) Wang, Y.; Lin, S.; Jiang, H.; Gu, Y.; Wu, Y.; Ma, J.; Ke, Y.; Zhang, L. W.; Wang, Y.; Gao, M. Visualizable Delivery of Nanodisc Antigen-Conjugated Adjuvant for Cancer Immunotherapy. *CCS Chem.* **2022**, *4* (4), 1238−1250.

(37) Williford, J.-M.; Ishihara, J.; Ishihara, A.; Mansurov, A.; Hosseinchi, P.; Marchell, T. M.; Potin, L.; Swartz, M. A.; Hubbell, J. A. Recruitment of CD103+ dendritic cells via tumor-targeted chemokine delivery enhances efficacy of checkpoint inhibitor immunotherapy. *Sci. Adv.* **2019**, *5* (12), No. eaay1357.

(38) Herrera, F. G.; Ronet, C.; Ochoa de Olza, M.; Barras, D.; Crespo, I.; Andreatta, M.; Corria-Osorio, J.; Spill, A.; Benedetti, F.; Genolet, R.; Orcurto, A.; Imbimbo, M.; Ghisoni, E.; Navarro Rodrigo, B.; Berthold, D. R.; Sarivalasis, A.; Zaman, K.; Duran, R.; Dromain, C.; Prior, J.; Schaefer, N.; Bourhis, J.; Dimopoulou, G.; Tsourti, Z.; Messemaker, M.; Smith, T.; Warren, S. E.; Foukas, P.; Rusakiewicz, S.; Pittet, M. J.; Zimmermann, S.; Sempoux, C.; Dafni, U.; Harari, A.; Kandalaft, L. E.; Carmona, S. J.; Dangaj Laniti, D.; Irving, M.; Coukos, G. Low Dose Radiotherapy Reverses Tumor Immune Desertification and Resistance to Immunotherapy. *Cancer Discovery* **2022**, *12* (1), 108−133.

(39) Cloughesy, T. F.; Mochizuki, A. Y.; Orpilla, J. R.; Hugo, W.; Lee, A. H.; Davidson, T. B.; Wang, A. C.; Ellingson, B. M.; Rytlewski, J. A.; Sanders, C. M.; Kawaguchi, E. S.; Du, L.; Li, G.; Yong, W. H.; Gaffey, S. C.; Cohen, A. L.; Mellinghoff, I. K.; Lee, E. Q.; Reardon, D. A.; O'Brien, B. J.; Butowski, N. A.; Nghiemphu, P. L.; Clarke, J. L.; Arrillaga-Romany, I. C.; Colman, H.; Kaley, T. J.; de Groot, J. F.; Liau, L. M.; Wen, P. Y.; Prins, R. M. Neoadjuvant anti-PD-1 immunotherapy promotes a survival benefit with intratumoral and systemic immune responses in recurrent glioblastoma. *Nat. Med.* **2019**, *25* (3), 477−486.

(40) Esteva, F. J.; Hubbard-Lucey, V. M.; Tang, J.; Pusztai, L. Immunotherapy and targeted therapy combinations in metastatic breast cancer. *Lancet Oncol.* **2019**, *20* (3), e175−e186.

(41) Pavlova, N. N.; Thompson, C. B. The Emerging Hallmarks of Cancer Metabolism. *Cell Metab.* **2016**, *23* (1), 27−47.

(42) Chong, M. F. F.; Hodson, L.; Bickerton, A. S.; Roberts, R.; Neville, M.; Karpe, F.; Frayn, K. N.; Fielding, B. A. Parallel activation of de novo lipogenesis and stearoyl-CoA desaturase activity after 3 d of high-carbohydrate feeding. *Am. J. Clin. Nutr.* **2008**, *87* (4), 817−823.

(43) Butler, L. M.; Perone, Y.; Dehairs, J.; Lupien, L. E.; de Laat, V.; Talebi, A.; Loda, M.; Kinlaw, W. B.; Swinnen, J. V. Lipids and cancer: Emerging roles in pathogenesis, diagnosis and therapeutic intervention. *Adv. Drug Delivery Rev.* **2020**, *159*, 245−293.

(44) Dmitrieva-Posocco, O.; Wong, A. C.; Lundgren, P.; Golos, A. M.; Descamps, H. C.; Dohnalová, L.; Cramer, Z.; Tian, Y.; Yueh, B.; Eskiocak, O.; Egervari, G.; Lan, Y.; Liu, J.; Fan, J.; Kim, J.; Madhu, B.; Schneider, K. M.; Khoziainova, S.; Andreeva, N.; Wang, Q.; Li, N.; Furth, E. E.; Bailis, W.; Kelsen, J. R.; Hamilton, K. E.; Kaestner, K. H.; Berger, S. L.; Epstein, J. A.; Jain, R.; Li, M.; Beyaz, S.; Lengner, C. J.; Katona, B. W.; Grivennikov, S. I.; Thaiss, C. A.; Levy, M. β-

Hydroxybutyrate suppresses colorectal cancer. *Nature* **2022**, *605* (7908), 160−165.

(45) Yang, W. S.; Kim, K. J.; Gaschler, M. M.; Patel, M.; Shchepinov, M. S.; Stockwell, B. R. Peroxidation of polyunsaturated fatty acids by lipoxygenases drives ferroptosis. *Proc. Natl. Acad. Sci. U. S. A.* **2016**, *113* (34), E4966−E4975.

(46) Gao, M.; Monian, P.; Quadri, N.; Ramasamy, R.; Jiang, X. Glutaminolysis and Transferrin Regulate Ferroptosis. *Mol. Cell* **2015**, *59* (2), 298−308.

(47) Ping, Y.; Shan, J.; Liu, Y.; Liu, F.; Wang, L.; Liu, Z.; Li, J.; Yue, D.; Wang, L.; Chen, X.; Zhang, Y. Taurine enhances the antitumor efficacy of PD-1 antibody by boosting CD8+ T cell function. *Cancer Immunol. Immunother.* **2023**, *72* (4), 1015−1027.

(48) Geeraerts, S. L.; Heylen, E.; De Keersmaecker, K.; Kampen, K. R. The ins and outs of serine and glycine metabolism in cancer. *Nat. Metab.* **2021**, *3* (2), 131−141.

(49) Wisniewski, J. R.; Zougman, A.; Nagaraj, N.; Mann, M. Universal sample preparation method for proteome analysis. *Nat. Methods* **2009**, *6* (5), 359−62.

(50) Gu, Y.; Zhou, Y.; Wu, Y.; Ma, J.; Wang, Y.; Wang, Q.; Wang, Y. Apoferritin-Engineered Nanoprobe for Tumor-Targeted Triple-NIR Imaging and Phototherapy. *Anal. Chem.* **2021**, *93* (25), 8835−8845.